Thermohaline and Wind Forcing of a Circumpolar Channel with Blocked Geostrophic Contours

DANIEL BOROWSKI, RÜDIGER GERDES, AND DIRK OLBERS

Alfred Wegener Institute for Polar and Marine Research, Bremerhaven, Germany

(Manuscript received 8 August 2001, in final form 12 February 2002)

ABSTRACT

The Antarctic Circumpolar Current is governed by unique dynamics. Because the latitude belt of Drake Passage is not zonally bounded by continents, the Sverdrup theory does not apply to the Antarctic Circumpolar Current. However, most of the geostrophic contours are blocked at Drake Passage, which provides an important dynamic constraint for the vorticity equation of the depth averaged flow.

This study addresses the effects of thermohaline and wind forcing on the large-scale transport of a circumpolar current with blocked geostrophic contours. Various numerical experiments with three different idealized model geometries were conducted. Based on the results and theoretical arguments, the authors promote an indirect wind effect on the circumpolar current: while the direct effects of the wind in driving the circumpolar current through a vertical transfer of the applied wind stress are of minor importance, the wind does substantially influence the circumpolar current transport through its effects on the density field.

This indirect wind effect is discussed in two steps. First, at the latitudes of the circumpolar current and longitudes where the geostrophic contours are blocked, the meridional gradient of the mass transport streamfunction is to leading order balanced by the meridional gradient of the baroclinic potential energy. This balance implies that the total transport is to leading order baroclinic and that the deep transport is small. For this statement, some theoretical arguments are offered. Second, a simplified analytical model is used to obtain the distribution of the baroclinic potential energy. Assuming an advective–diffusive balance for the densities in the deep downwelling northern branch of the Deacon cell, this model reproduces the qualitative dependence of the circumpolar current transport on the imposed wind and thermohaline forcing as well as on the turbulent diffusivities.

1. Introduction

In recent years much interest has been attributed to the effects of topography and stratification on the transport of the Antarctic Circumpolar Current (ACC). Attention has been drawn to the question of how the circulation can decouple from the contours of f/H (e.g., Marshall 1995; Krupitsky et al. 1996; Ivchenko et al. 1999) and how the momentum input by surface wind stress can be transferred down to the ocean floor (e.g., Johnson and Bryden 1989; Treguier and McWilliams 1990; Wolff et al. 1991; Ivchenko et al. 1996; Olbers 1998; Völker 1999). Taking a slightly different perspective, Olbers and Wübber (1991), Cai and Baines (1996), Samelson (1999), Gnanadesikan and Hallberg (2000), and Gent et al. (2001) pointed out the active role of stratification in driving the ACC. The physical mechanism discussed in the last few papers is appealingly simple (basically geostrophy), evidence from numerical models can be found as early as in Gill and Bryan (1971), and the theoretical concepts involved have been known for a long time (e.g., Rattray and Dworski 1978; Mertz and Wright 1992).

Samelson (1999) proposed a simple analytical theory for the steady-state, large-scale geostrophic circulation of a stratified fluid in the Gill and Bryan (1971) geometry of a rectangular basin with a circumpolar connection. The abyssal interior fluid is assumed to be stagnant and the thermal wind equation is applied to determine the channel transport. Besides convective adjustment to maintain static stability, Samelson (1999) neglected mixing of tracers all together. Thus he found the vertical structure of the stratification to depend on the imposed thermal surface forcing and the geometry but not on the wind forcing, and he did not observe any influence of the wind forcing on the channel transport. However, Toggweiler and Samuels (1995, 1998), McDermott (1996), Gnanadesikan (1999), and Vallis (2000) discuss how the wind affects deep stratification, which in turn would influence the baroclinic contribution to the channel transport as well.

In their illustrative numerical study Cai and Baines (1996) observed strong interactions between the thermohaline and the wind-driven circulation in the South-

Corresponding author address: Daniel Borowski, Alfred Wegener Institute for Polar and Marine Research, Bussestrasse 24, Bremerhaven 27570, Germany.
E-mail: borowski@awi-bremerhaven.de

ern Ocean. Driving an ocean model both by thermohaline (restoring to SST and SSS) and wind forcing, they obtained an ACC with a depth-integrated transport significantly stronger than the sum of the transport of a pure wind-driven (homogeneous) and a pure thermohaline driven ocean model. By analyzing the zonally and vertically integrated momentum balance, Cai and Baines (1996) identified the bottom form stress as the term responsible for driving the ACC in the pure thermohaline driven ocean. Considering the case of a thermohaline and wind-driven ocean, Cai and Baines (1996) argued that, while the direct effect of the wind forcing on the ACC is small, a wind-induced enhancement of the bottom form stress could be responsible for the additional forcing driving the ACC. Though this numerical study is an enlightening demonstration of an indirect wind effect on the ACC, the physical explanation must be rejected. The proposed mechanism of a bottom form stress driving the ACC and lateral friction balancing the bottom form stress is inconsistent with the findings of Wolff et al. (1991), Stevens and Ivchenko (1997), and Gille (1997) in eddy-resolving models, which support the balance proposed by Munk and Palmén (1951) instead. The balance found by Cai and Baines (1996) must be ascribed to the unrealistic strong lateral friction used in this study.

More recently, Gnanadesikan and Hallberg (2000) investigated the effects of Southern Hemisphere winds on the ACC using a two-layer model with interface restoring and a coarse-resolution general circulation model. They argued that the northward Ekman flux of light water connected with increased eastward winds within the Southern Ocean would produce a deeper pycnocline and warmer deep water in the subtropics of the Southern Hemisphere. This in turn results in a much larger thermal wind shear across the Circumpolar Current. By assuming relatively small near-bottom velocities an increase in ACC transport can be derived. Their discussion of the dynamical balance left one question open: the assumption of a nearly motionless abyss might be consistent with model results and observations, but nevertheless it would be desirable to give dynamical reasons for the claim that the contribution of the bottom flow to the ACC transport is negligible.

In this paper we investigate the effects of the thermohaline and the wind forcing on the large-scale steady-state transport in a circumpolar channel with blocked geostrophic contours (i.e., contours of f/H), which serves as a model of the ACC. This is done by using three coarse-resolution general circulation models with different geometries and by employing some analytical arguments to the model geometries. In particular, we support an indirect wind effect similar to the one proposed by Gnanadesikan and Hallberg (2000), but treat matters differently in two important respects: first, instead of using the assumption of a motionless abyss, we work out some consequences of blocked geostrophic contours and vorticity conservation. Thereby we offer a more complete discussion of the dynamic balance in section 2. Second, we treat the thermodynamic balance in a more simplified way. We disregard the possible feedback of the Southern Ocean winds through their impact on the North Atlantic Deep Water formation and focus on the wind effects that take place mainly within the Southern Ocean region. This simplified treatment in section 3 allows us to formulate a simple analytical model, which is able to reproduce the qualitative dependence of the channel transport on wind forcing, thermohaline forcing, and diffusion parameters.

2. The dynamic balance

a. Blocked geostrophic contours in the Southern Ocean

Geostrophic contours (i.e., contours of constant f/H, where f is the Coriolis frequency and H the ocean depth) are important dynamic characteristics for the depth integrated flow. In the absence of baroclinicity and forcing, the depth-integrated flow would have to follow geostrophic contours, but in a stratified ocean the circulation can decouple from the geostrophic contours. Due to vorticity conservation, any transport across geostrophic contours must be dynamically balanced—by baroclinic effects, Ekman pumping, or other effects (see section 2c).

Figure 1 shows the geostrophic contours in the Southern Ocean. There are two prominent regions where geostrophic contours are blocked by continents: The region between Australia and Antarctica, and Drake Passage between South America and Antarctica. Here, the ACC must cross geostrophic contours. Although the geostrophic contours are not blocked there, the ACC also crosses the geostrophic contours at the East Pacific Rise and several other locations.

In the following we shall use an idealized model of a channel flow across topography. The model includes the important dynamical feature: that the geostrophic contours are blocked at the topographic obstacle.

b. A zonally periodic channel with topography

The idealized model is a zonally periodic channel (see Fig. 2) that extends from 55° to 65°S and covers 80° longitude. The depth of the channel is 4000 m, and a meridional ridge with a zonal extent of L is arranged to block the deep part of the passage. At the center of the ridge the depth reduces to H_{top}, where three different values have been used in various configurations (see Table 1). In all configurations, the geostrophic contours are blocked at the ridge (as sketched in Fig. 3) and the channel flow must cross the geostrophic contours at the ridge.

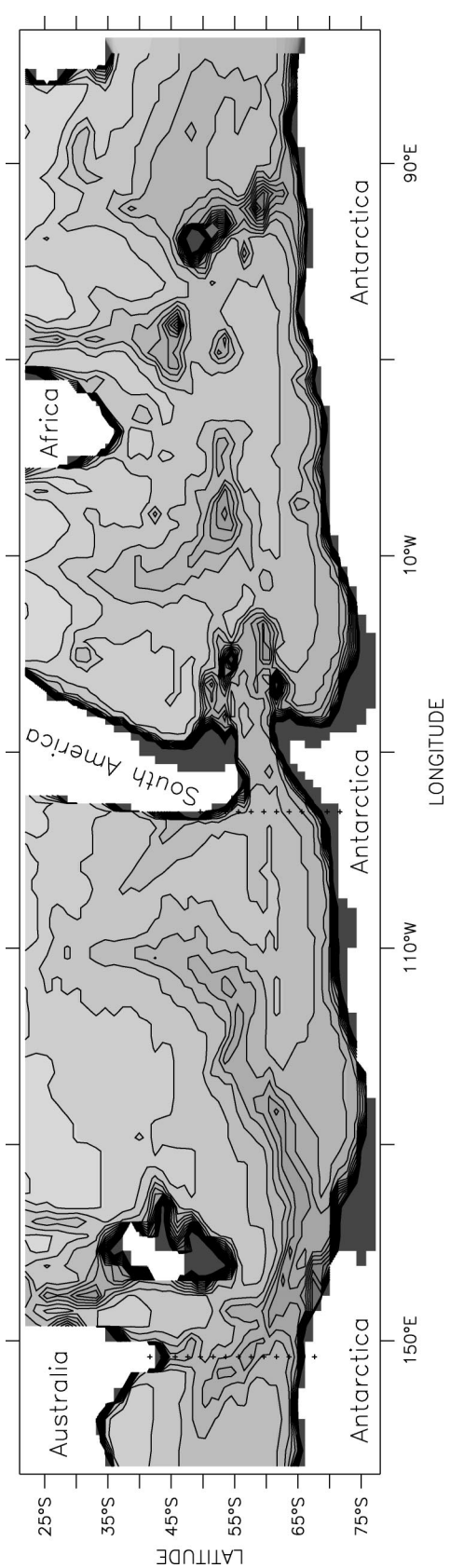

FIG. 1. Geostrophic contours (f/H) in the Southern Ocean. The geostrophic contours are blocked at the Drake Passage between South America and Antarctica. The ACC must thus cross the geostrophic contours at Drake Passage. This is also the case in the region between Australia and Antarctica, and at the Kerguelen Plateau.

c. Vorticity conservation and channel transport

The transport across geostrophic contours is constrained by the vorticity equation of the depth-averaged flow. Assuming the hydrostatic approximation, the Boussinesq approximation, as well as the rigid-lid approximation, and summarizing the frictional and the nonlinear terms in a vector **G**, the steady-state vorticity equation of the depth-averaged flow can be written as

$$\nabla\frac{f}{H}\cdot\mathbf{U} = J\left(\chi, \frac{1}{H}\right) + \frac{f}{H}\nabla\cdot\mathbf{U}_{\mathrm{Ek}} + \nabla\frac{f}{H}\cdot\mathbf{U}_{\mathrm{Ek}} + \mathrm{curl}_z\left(\frac{\mathbf{G}}{H}\right), \tag{1}$$

where we are using the vertically integrated transport **U**, the baroclinic potential energy χ, and the Ekman transport $\mathbf{U}_{\mathrm{Ek}}$:

$$\mathbf{U} = \int_{-H}^{0}\mathbf{u}\,dz = \mathbf{k}\times\nabla\Psi; \qquad \chi = \frac{g}{\rho_0}\int_{-H}^{0} z\rho'\,dz;$$

$$\mathbf{U}_{\mathrm{Ek}} = -\frac{1}{\rho_0 f}\mathbf{k}\times\boldsymbol{\tau}.$$

Here $J(A, B)$ is the Jacobian of A and B, **u** the horizontal velocity field, Ψ the streamfunction, g is the gravitational acceleration, ρ' the density ρ minus a horizontal mean density profile $\overline{\rho}$, ρ_0 a constant reference density, $\boldsymbol{\tau}$ the surface wind stress, z the vertical coordinate, and **k** the unit vertical vector.

Equation (1) expresses the transport across geostrophic contours (lhs) in terms of the JEBAR term (first term on the rhs), the divergence of the Ekman transport (second term on the rhs), the Ekman transport across geostrophic contours (third term on the rhs), and frictional as well as non linear effects (last term on the rhs). We assume that frictional and nonlinear effects can only become relevant within narrow boundary layer currents. Thus **G** can be neglected in the interior. The joint effect of baroclinicity and relief (JEBAR) is discussed for example, in Mertz and Wright (1992); it represents the difference between the bottom pressure torque and that which would occur if bottom pressure gradients were equal to depth-averaged pressure gradients. In the case of blocked geostrophic contours (as assumed in this paper) the complete transport through the channel must be balanced by the terms on the rhs of (1).

The question then is, which of the rhs terms of (1) can generate a substantial transport not only across geostrophic contours but also across the meridional ridge of the channel. Figure 4 is an illustration of (1). If there is any transport across the meridional ridge, the lhs of (1) must change sign at the top of the ridge. This is sketched in the upper-left panel of Fig. 4. Thus, in order to obtain a substantial transport across the ridge, the rhs of (1) must change sign in a corresponding manner. This

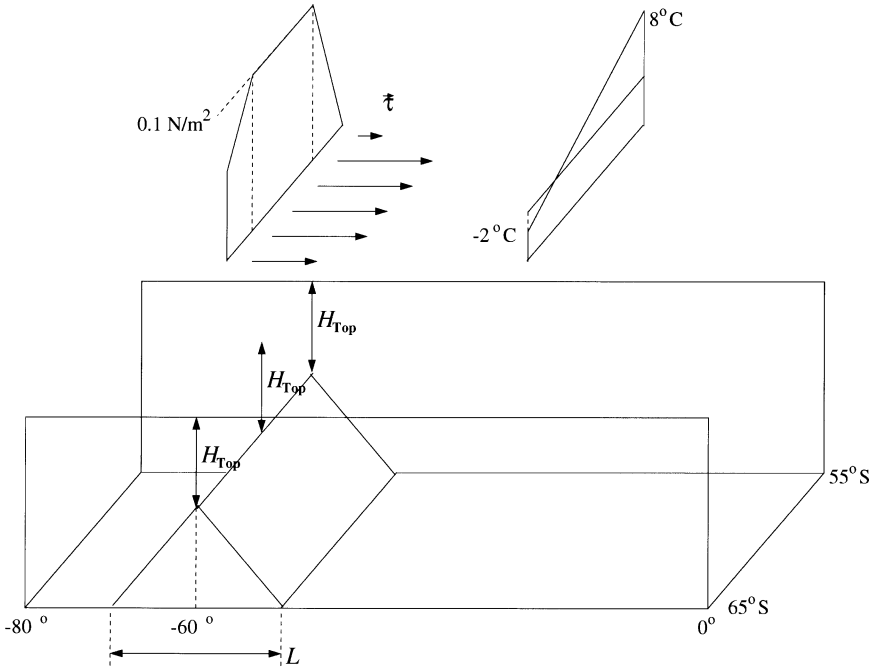

FIG. 2. Geometry of the zonally periodic channel with topography. The flow in this channel is forced by eastward wind stress and an imposed south–north temperature gradient at the surface (see upper panel). The channel flow must cross the geostrophic contours that are blocked at the topographic barrier.

must be due to one or more of the following effects expressed by the terms of the rhs.

- *JEBAR.* With a predominantly meridional density gradient (as found in the climatological state of the ACC) the JEBAR term changes sign at the top of the ridge (see upper-right panel of Fig. 4). Thus a flow across the meridional ridge (as sketched in the upper-left panel of Fig. 4) can be balanced by the JEBAR term, and a substantial circumpolar channel transport can be generated by meridional density gradients.
- *Ekman divergence.* Assuming an upward Ekman pumping within the whole area of the channel (see lower-right panel of Fig. 4), the Ekman divergence has an uniform sign. The resulting flow would converge over the meridional ridge, but would not cross it (lower-left panel of Fig. 4). In order to obtain a substantial circumpolar transport across the ridge, one would either need to include further effects (e.g., frictional effects within boundary layer currents), or a special wind stress field, where the Ekman divergence term would change the sign in a manner suitable to the topography. The transport within a homogeneous, zonally periodic β channel with topography (similar to the one used here), where the current is driven by Ekman pumping, was investigated by Krupitsky and Cane (1994) and Wang and Huang (1995). They obtained a circumpolar channel current that was mainly restricted to very narrow frictional boundary layer currents at the southern and northern walls, joined by a narrow jet along a particular geostrophic contour. Choosing a ridge height of a realistic value for the Southern Ocean, the models of Krupitsky and Cane (1994) and Wang and Huang (1995) would lead to a channel transport of only a few Sverdrups, which is not realistic for the ACC transport.
- *Ekman transport.* The Ekman transport across geostrophic contours [third term on the rhs of (1)] can in principle generate a transport across the meridional ridge. But assuming, consistent with the conditions within the Southern Ocean, a wind stress that is mostly eastward, the Ekman transport is mostly northward. In such a case it does not substantially contribute to the channel transport.

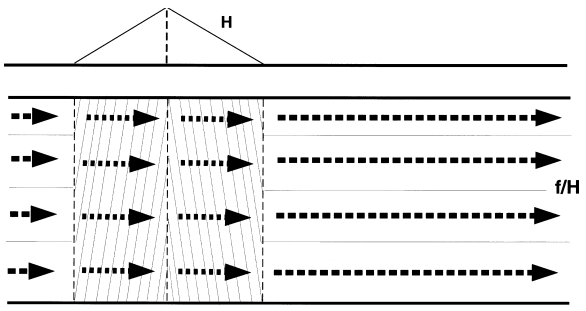

FIG. 3. Topography H (upper panel) and geostrophic contours f/H (thin solid lines, lower panel) of the zonally periodic channel with topography (Fig. 2). At the topographic obstacle, the circumpolar current within this channel (dashed arrows) must cross geostrophic contours.

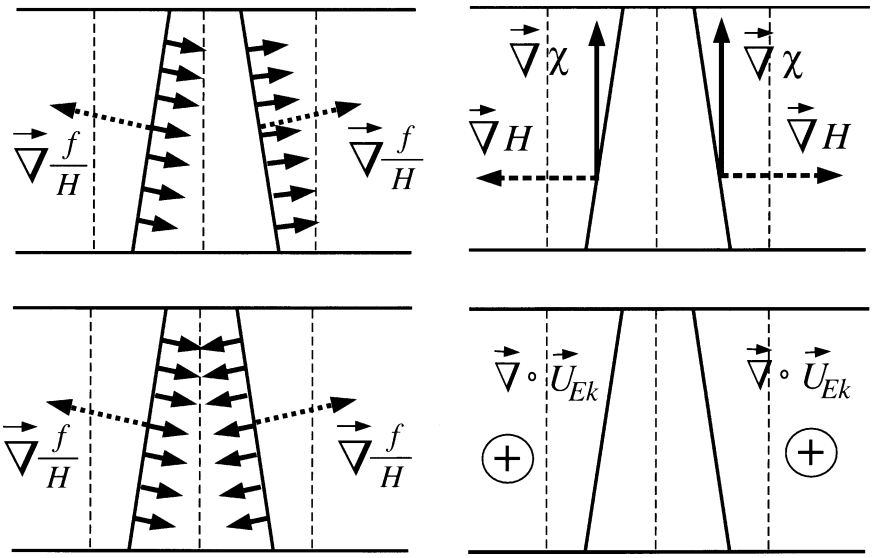

FIG. 4. Illustration of Eq. (1) for the zonally periodic channel. All four panels show two selected geostrophic contours (thick solid diagonal lines) at the meridional ridge (indicated by thin dashed vertical lines; cf. Fig. 3). The two left panels illustrate the lhs of (1). The dashed arrows display the gradient of f/H and the normal components of the transport across geostrophic contours are sketched by the small solid arrows. The upper-left panel depicts the case where the lhs of (1) changes sign at the top of the ridge, and the lower-left panel the case where the sign of the lhs of (1) remains constant. The JEBAR term is sketched in the upper-right panel (where dense water is assumed at the south, near the pole, and lighter water is assumed to the north, toward the equator). ∇H changes sign at the top of the meridional ridge and thus the JEBAR term changes sign, too. In the lower-right panel the second term of the rhs of (1) is sketched for the case of upward Ekman pumping within the whole area. The sign of this term is constant. A forcing as sketched in the upper-right panel would result in a flow as sketched in the upper-left panel, and a forcing as sketched in the lower-right panel would result in a flow as sketched in the lower-left panel.

- *Nonlinear and frictional effects.* Nonlinear and frictional effects can be relevant within boundary layer currents only. They are dominant in the experiments of Krupitsky and Cane (1994) and Wang and Huang (1995), where the channel transport occurs in the boundary layers. However, in the numerical model experiments considered in the present paper, a dynamic regime is realized in which the transport is not dominated by boundary currents, and thus the nonlinear and frictional terms turned out to be (to leading order) negligible in the dynamic balance (see sections 2e, 2f, and 3a).

Concluding the discussion above, we suggest that a circumpolar current with blocked geostrophic contours can most efficiently be driven by meridional density gradients, and the channel transport is to leading order determined by the distribution of the baroclinic potential energy χ. At the meridional ridge, where the geostrophic contours are blocked, we propose an approximate balance of the transport across geostrophic contours and the JEBAR term:

$$\nabla \frac{f}{H} \cdot \mathbf{U} = J\left(\Psi, \frac{f}{H}\right) \approx J\left(\chi, \frac{1}{H}\right). \tag{2}$$

A circumpolar current that is dominantly driven by baroclinic effects is consistent with the findings of Gill and Bryan (1971), Olbers and Wübber (1991), Marshall (1995), Cai and Baines (1996), Samelson (1999), and Gnanadesikan and Hallberg (2000).

d. Shear transport and deep transport

Among others, Samelson (1999) and Gnanadesikan and Hallberg (2000) estimated the transport of the Antarctic Circumpolar Current using the thermal wind equation. If the abyssal velocities are small compared to the depth averaged velocities, this approach will lead to satisfactory results. However, Samelson (1999) and Gnanadesikan and Hallberg (2000) did not provide any dynamical arguments as to why the abyssal velocities should be small. Here, we promote some ideas concerning the deep flow and give an estimate for the deep transport across geostrophic contours. Since the ACC must cross the geostrophic contours at some locations within the Southern Ocean, the transport across the geostrophic contours is relevant.

Now, using the thermal wind balance, the depth-integrated shear transport $\mathbf{U}_{\text{shear}}$ (relative to the bottom layer) is written as

$$\mathbf{U}_{\text{shear}} = \frac{1}{f}\mathbf{k} \times \left(\nabla \chi + \frac{gH}{\rho_0}\rho_b \nabla H\right), \tag{3}$$

and the deep geostrophic transport $\mathbf{U}_{\text{deep}}$ (geostrophic bottom velocity times depth) is given by

$$\mathbf{U}_{\text{deep}} = \frac{H}{\rho_0 f}\mathbf{k} \times (\nabla p)_b, \tag{4}$$

where $\rho_b = \rho'(z = -H)$ is the bottom density, p the pressure, and $(\nabla p)_b$ the horizontal pressure gradient at the bottom. (Note $(\nabla p)_b + g\rho_b \nabla H = \nabla p_b$, where p_b is the bottom pressure.) The depth-integrated momentum balance takes the form

$$f\nabla\Psi = \nabla\chi + \frac{gH}{\rho_0}\rho_b\nabla H + \frac{H}{\rho_0}(\nabla p)_b - \frac{1}{\rho_0}\boldsymbol{\tau} + \mathbf{G}. \tag{5}$$

The curl of $1/H$ times this equation results in the voriticty balance (1). The momentum balance (5), on the other hand, may be expressed in terms of transports if one writes the total depth-integrated transport $\mathbf{U} = \mathbf{k} \times \nabla\Psi$ as the sum of the shear transport $\mathbf{U}_{\text{shear}}$, the deep transport $\mathbf{U}_{\text{deep}}$, the Ekman transport $\mathbf{U}_{\text{Ek}}$, and an additional term allowing for nonlinear and frictional effects:

$$\mathbf{U} = \mathbf{U}_{\text{shear}} + \mathbf{U}_{\text{deep}} + \mathbf{U}_{\text{Ek}} + \left(\frac{1}{f}\mathbf{k} \times \mathbf{G}\right). \tag{6}$$

Evaluation of the divergence of (6) yields an expression for the deep transport across geostrophic contours:

$$\nabla\frac{f}{H} \cdot \mathbf{U}_{\text{deep}} = -\frac{1}{H}\nabla f \cdot \mathbf{U}_{\text{shear}} + \frac{f}{H}\nabla \cdot \mathbf{U}_{\text{Ek}} + \frac{f}{H}\,\text{curl}_z\left(\frac{\mathbf{G}}{f}\right). \tag{7}$$

The deep geostrophic transport across geostrophic contours is thus induced by the meridional component of the shear transport, the divergence of the Ekman transport, and frictional as well as nonlinear effects. Adding $\nabla(f/H) \cdot \mathbf{U}_{\text{shear}}$ to both sides of (7) we obtain

$$\nabla\frac{f}{H} \cdot \mathbf{U} = -\frac{f}{H^2}\nabla H \cdot U_{\text{shear}} + \frac{f}{H}\nabla \cdot \mathbf{U}_{\text{Ek}} + \frac{f}{H}\,\text{curl}_z\left(\frac{\mathbf{G}}{f}\right), \tag{8}$$

and the ratio of (7) and (8) gives

$$\frac{\nabla\frac{f}{H} \cdot \mathbf{U}_{\text{deep}}}{\nabla\frac{f}{H} \cdot \mathbf{U}} = \frac{\frac{1}{f}\nabla f \cdot \mathbf{U}_{\text{shear}} - \Gamma}{\frac{1}{H}\nabla H \cdot \mathbf{U}_{\text{shear}} - \Gamma} \tag{9}$$

with

$$\Gamma = \nabla \cdot \mathbf{U}_{\text{Ek}} + \text{curl}_z\left(\frac{\mathbf{G}}{f}\right).$$

From (9) one can see:

1) if the shear transport $\mathbf{U}_{\text{shear}}$ is parallel to geostrophic contours, then the total transport across geostrophic contours can be completely found in the deep transport [i.e., lhs of (9) = 1];
2) if the divergence of the Ekman transport plus the fricitonal and nonlinear terms are negligible (i.e., Γ is small), then a zonal shear transport $\mathbf{U}_{\text{shear}}$ leads to a small contribution of the deep transport to the total transport across geostrophic contours [i.e., small lhs of (9)];
3) if the term Γ is small, then a shear transport $\mathbf{U}_{\text{shear}}$, which is parallel to topographic contours, leads to a large contribution of the deep transport to the total transport across geostrophic contours (i.e., large lhs);
4) if $\Gamma = 0$ and the transport $\mathbf{U}_{\text{shear}}$ is parallel to contours of f/H^{α}, then lhs = α.

The Ekman transport $\mathbf{U}_{\text{Ek}}$ is about two orders of magnitude smaller than the shear transport $\mathbf{U}_{\text{shear}}$, and the frictional and nonlinear effects are, by assumption, considered negligible outside boundary layer currents. Thus Γ can be considered small, and the lhs of (9) is small if $\mathbf{U}_{\text{shear}}$ is ''closer'' to zonal than to following f/H contours, in the sense defined by (4) above, that is, if α is close to zero. In the numerical experiments of the present paper, this condition is met at the meridional ridge of the stratified, zonally periodic channel (see section 2e and Fig. 8), as well as at some locations (relevant to our discussion) in the model with more realistic topography (see section 2f). At these locations, we do expect, from the discussion above, a small deep transport across geostrophic contours compared to the total transport across geostrophic contours.

So far, only the component of the deep transport across geostrophic contours has been considered. Its component along geostrophic contours does not enter the arguments above. However, concentrating on the regions where the geostrophic contours are blocked, the component across the geostrophic contours is the relevant component for the circumpolar transport. Thus in the regions where 1) the lhs of (9) is small, 2) the geostrophic contours are blocked, 3) the Ekman transport is small compared to the total transport, and 4) nonlinear and frictional effects can be disregarded, the total transport (or at least the component of the total transport that contributes to the circumpolar transport) can be estimated by the shear transport,

$$\mathbf{U} \approx \mathbf{U}_{\text{shear}}, \tag{10}$$

which can be equivalently expressed in the form

$$f\nabla\Psi \approx \nabla\chi + \frac{gH}{\rho_0}\rho_b\nabla H. \tag{11}$$

Similar ideas concerning the smallness of the bottom flow are put forwards in Hughes and Killworth (1995).

Provided the channel is bounded by vertical walls, replacing f by a constant f_0 (taken at a central latitude) and integrating (11) along a topographic contour from

TABLE 1. Configurations used for the numerical experiments with the channel geometry (see Fig. 2).

Configuration	Geometric ridge parameters: Zonal extent L (°)	Geometric ridge parameters: Depth H_{top} (m)	Imposed forcing: Wind	Imposed forcing: Thermohaline
C1a	20	1000	yes	yes
C2a	20	2000	yes	yes
C3a	20	3000	yes	yes
C1b	20	1000	no	yes
C2b	20	2000	no	yes
C3b	20	3000	no	yes
C1h	20	1000	yes	no
C2h	20	2000	yes	no
C3h	20	3000	yes	no
C4a	40	1000	yes	yes
C5a	40	2000	yes	yes
C6a	40	3000	yes	yes
C4b	40	1000	no	yes
C5b	40	2000	no	yes
C6b	40	3000	no	yes
C4h	40	1000	yes	no
C5h	40	2000	yes	no
C6h	40	3000	yes	no

the southern to the northern channel boundary gives an approximate balance for the channel transport $\Delta\Psi$:

$$\Delta\Psi \approx \frac{\Delta\chi}{f_0}. \tag{12}$$

The balance (11) is the central result of this section. It is important for at least two reasons. First, it allows to calculate the barotropic transport in the case of blocked geostrophic contours from the density field alone. Second, it implies that the strength of the ACC at, say, Drake Passage is determined by the processes that establish the large-scale density structure, especially the meridional density gradient. In section 2e and 2f, the balance (11) is compared with numerical results of a large suite of experiments.

e. Numerical experiments with the channel model

To test the validity of (11) and the arguments of the preceding subsections concerning the dynamical balance, we conducted numerical experiments with a three-dimensional primitive equation model [Second Modular Ocean Model (MOM 2); see Pacanowski 1995] and with the geometry specified in section 2b. Because the density field, especially the deep density field, governs (11) we need integration times long enough for the density field to adjust to the imposed surface forcing. Thus, a coarse-resolution model is necessary, although eddy effects that could be important in the ACC are then neglected. The horizontal resolution is $1° \times 2°$ (meridional $\times$ zonal) and the length and width of the channel are 80° in longitude and 10° in latitude, respectively; the vertical is resolved by 16 levels with a spacing varying from 34 m at the surface to 300 m at depth 1002-m and an uniform spacing of 300 m below 1002 m down to 4002 m. The parameters of the turbulent viscosity are 10^5 m^2 s^{-1} in the lateral and 10^{-3} m^2 s^{-1} in the vertical direction, and the turbulent diffusivity was set to 10^{-4} m^2 s^{-1} in both lateral and vertical directions. The flux-corrected transport (FCT) scheme (Gerdes et al. 1991) was applied, which allows the use of very small lateral turbulent diffusivities. In order to minimize the integration time necessary to obtain an approximate steady state, the distorted physics technique of Bryan (1984) was applied and different time steps for the tracer and momentum variables were chosen.

TABLE 2. Results from the numerical experiments with the channel model, using the configurations specified in Table 1. The table compares the channel transport $\Delta\Psi$ and the baroclinic potential energy difference $\Delta\chi/f_0$ [f_0 is the Coriolis parameter at a central latitude (60°S)]. See Fig. 5 for a graphical comparison.

Configuration	$\Delta\chi/f_0$ (Sv)	$\Delta\Psi$ (Sv)	Configuration	$\Delta\chi/f_0$ (Sv)	$\Delta\Psi$ (Sv)
Thermohaline and wind forcing					
C1a	61.23	65.47	C4a	41.78	43.70
C2a	88.26	89.38	C5a	88.08	89.06
C3a	91.85	89.18	C6a	90.72	88.13
Only thermohaline forcing					
C1b	12.71	13.27	C4b	11.74	12.36
C2b	12.60	12.56	C5b	13.75	13.87
C3b	9.706	8.081	C6b	10.90	9.589
Only wind forcing					
C1h	0.000	1.187	C4h	0.000	0.791
C2h	0.000	2.966	C5h	0.000	2.745
C3h	0.000	9.664	C6h	0.000	8.976

Various numerical experiments were conducted, switching the thermohaline and the wind forcing on and off, as well as using different values for the geometric parameters L and H_{top} of the meridional ridge. All experiments started with a homogeneous channel at rest and were then integrated for 2000 years to a near-steady state. In the configurations with wind forcing, a zonally constant zonal wind stress with a maximum of 0.1 N m^{-2} is applied (see upper panel of Fig. 2), and for the configurations with thermohaline forcing, the surface temperature is restored to a linear function of latitude with -2°C at 65°S and 8°C at 55°S, while the salinity was kept constant at 34 psu. In the configurations without thermohaline forcing, homogeneous density with a constant potential temperature of 4°C and a constant salinity of 34 psu is used. The configurations are summarized in Table 1. The results of the numerical experiments are summarized in Table 2 and Figs. 5 and 6.

Figure 7 shows the streamfunction Ψ for the configuration C2h, in which the thermohaline forcing is switched off and the channel flow is driven by wind stress only. Consistent with the results of Krupitsky and Cane (1994) and Wang and Huang (1995) and the discussion of section 2c, the current is concentrated in boundary layers. Table 2 and Fig. 5 indicate a channel transport of only a few Sverdrups for the experiments with homogeneous density.

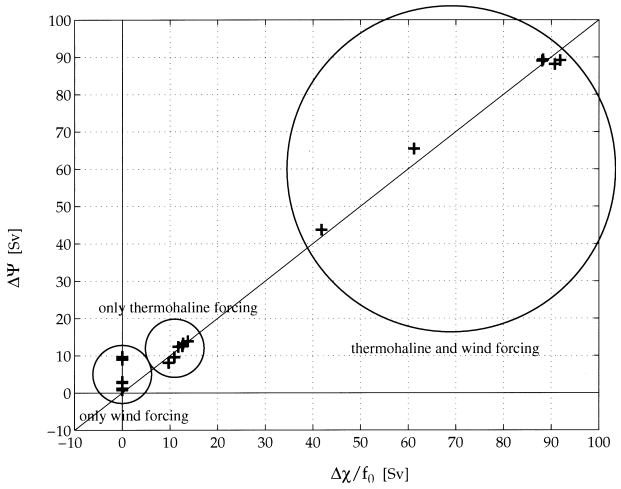

FIG. 5. Results from the numerical experiments with the channel model, using the configurations specified in Table 1. The plot compares the channel transport $\Delta\Psi$ and the baroclinic potential energy difference $\Delta\chi/f_0$, and indicates the experiments with ''only wind forcing,'' ''only thermohaline forcing,'' and ''thermhaline and wind forcing'' (cf. Table 2).

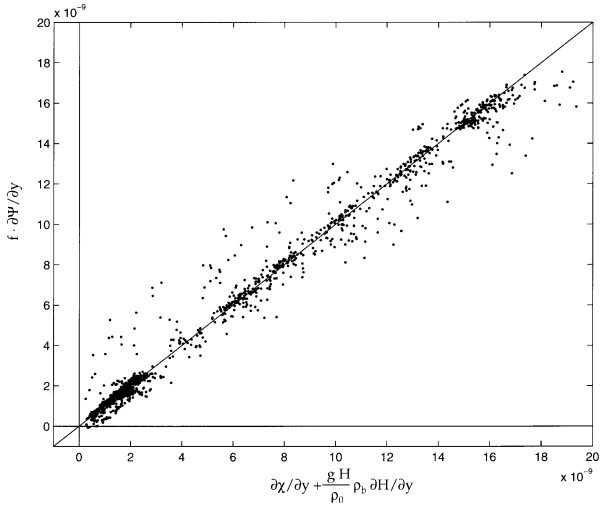

FIG. 6. Scatterplot of (11) for the numerical experiments with the channel model, where thermohaline forcing was included. In this scatterplot, (11) was evaluated for all grid points above the topographic barrier blocking the geostrophic contours.

In contrast, a substantial channel transport can be obtained by adding thermohaline forcing. Figure 8 shows the streamfunction Ψ and the baroclinic potential energy χ/f_0 for the configuration C2a, where thermohaline and wind forcing are used. The comparison shows an approximate correspondence of both fields. While there are small-scale deviations of χ/f_0 from the streamfunction Ψ in the area of the ridge, the over all transport $\Delta\Psi$ through the channel is very well captured by $\Delta\chi/f_0$. This holds for all experiments with thermohaline forcing (see Table 2 and Fig. 5). Both quantities differ by only a few Sverdrups for all topographic parameters used and for wind and no wind cases. The scatterplot of the lhs of (11) against the rhs (Fig. 6) demonstrates that the balance (11) holds in these experiments.

f. A global model with realistic topography

It remains to be shown that (11) is useful under realistic conditions. Therefore additional experiments were conducted using a global model with realistic topography (Fig. 9). To adequately resolve the topographic features in the Southern Ocean and especially at Drake Passage, a spatially varying horizontal resolution is used. In the vicinity of Drake Passage the resolution is $1^\circ \times 2^\circ$ (meridional $\times$ zonal), whereas it is $3^\circ \times 4^\circ$ in the northern Pacific. The meridional extent of the model is limited by solid walls at 78°N and 78°S, where restoring zones have been supplemented, to maintain realistic water mass properties in the deep ocean. The vertical is resolved by 25 levels with a vertical spacing varying from 30 m at the surface to 300 m at a depth of 2475 m and a uniform vertical spacing of 300 m down to 5475 m. The vertical turbulent viscosity is set to 10^{-3} m^2 s^{-1}, and the horizontal turbulent viscosity is proportional to the cube of the horizontal grid resolution Δx, where 10^4 m^2 s^{-1} is the value at $\Delta x = 100$ km. This allows a sufficient resolution of the boundary layers as well as an optimal use of the enhanced horizontal resolution at Drake Passage. The vertical hybrid mixing scheme of Bryan and Lewis (1979), the FCT scheme discussed by Gerdes et al. (1991), and the isopycnal thickness mixing parameterization of Gent and McWilliams (1990) were implemented. An isopycnal diffusivity of 10^3 m^2 s^{-1} was chosen and the isopycnal thickness diffusion coefficient was set to 10^2, 5×10^2, or 10^3 m^2 s^{-1} for different numerical experiments (see Table 3). Surface temperatures and salinities are restored to annual mean values from Levitus (1982). Hellerman and Rosenstein (1983) annual mean wind stresses are applied at the surface. In each numerical experiment the

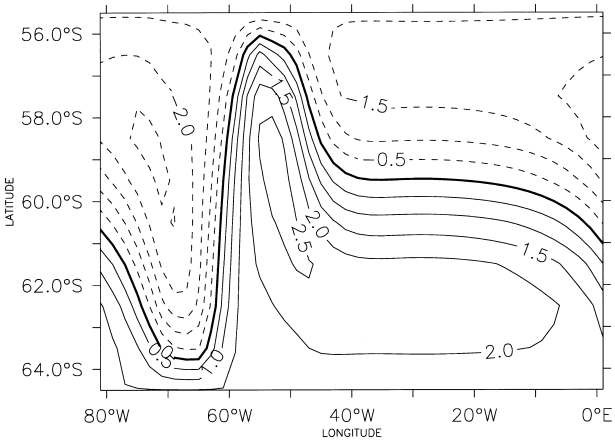

FIG. 7. Streamfunction Ψ in Sv for the configuration C2h (homogeneous channel with wind forcing only; see Table 1).

model was first initialized with the Levitus (1982) climatology and then run for 100 years, where again the distorted physics technique of Bryan (1984) was applied. While the adjustment of the deep density field to the surface forcing is clearly not finished after 100 years the velocity field can be considered to be in equilibrium with the density field and wind forcing, thus the validity of (11) can be tested already. The configurations and results of the experiments conducted are summarized in Table 3 and Figs. 10 and 11.

The bottom topography of the global model is much more complicated than the one of the channel model of section 2e. An integration of (11) along topographic contours to obtain (12) is not straightforward, and thus a direct comparison of the streamfunction Ψ with the baroclinic potential energy χ (as done for the channel model) is not appropriate for the global model. A reconstruction of the streamfunction Ψ can instead be obtained by integrating the meridional component of (11) in the meridional direction:

$$\Psi_{\text{reconstruction}} = \Psi_{y_{\text{south}}} + \int_{y_{\text{south}}}^{y_{\text{north}}} \frac{1}{f}\left(\frac{\partial \chi}{\partial y} + \frac{gH}{\rho_0}\rho_b \frac{\partial H}{\partial y}\right) dy. \quad (13)$$

The streamfunction Ψ and the reconstruction of the streamfunction by (13) are compared in the top two panels of Fig. 12. While there are clear differences in the closed basins of the major oceans, the overall agreement of the streamfunction and its reconstruction is rather good within the ACC region. This agreement is not trivial. As argued in section 2d, the total transport $\mathbf{U}$ can be obtained from the thermal wind equation if one can assume that the deep transport $\mathbf{U}_{\text{deep}}$ is negligible. This would immediately give (13) and $\Psi_{\text{reconstruction}}$ can be considered as the integral of the shear transport $\mathbf{U}_{\text{shear}}$. Clearly the deep transport $\mathbf{U}_{\text{deep}}$ is not negligible everywhere in the ocean. In section 2d, we found that the deep transport across geostrophic contours is small compared to the total transport across geostrophic contours if the shear transport is ''closer'' to zonal than to following geostrophic contours. At locations where the ACC has to cross the geostrophic contours this is the criterion that must be considered; see Figs. 1 and 12.

In section 2a, two regions were identified where the ACC must cross geostrophic contours: Drake Passage and the region between Australia and Antarctica. In these regions the above criterion is mostly satisfied, with few exceptions: east of Drake Passage, the ACC bends to the north into the Malvinas/Falkland Current and there the flow is not zonal at all. Consequently the deep transport is responsible for more than 25% of the total transport of the Malvinas/Falkland Current (see lower panel of Fig. 12). In the western part of Drake Passage the ACC is nearly zonal, and in this region the deep transport contributes less than 10% to the total transport. In the region between Australia and Antarctica the shear transport has a meridional component, though moderate

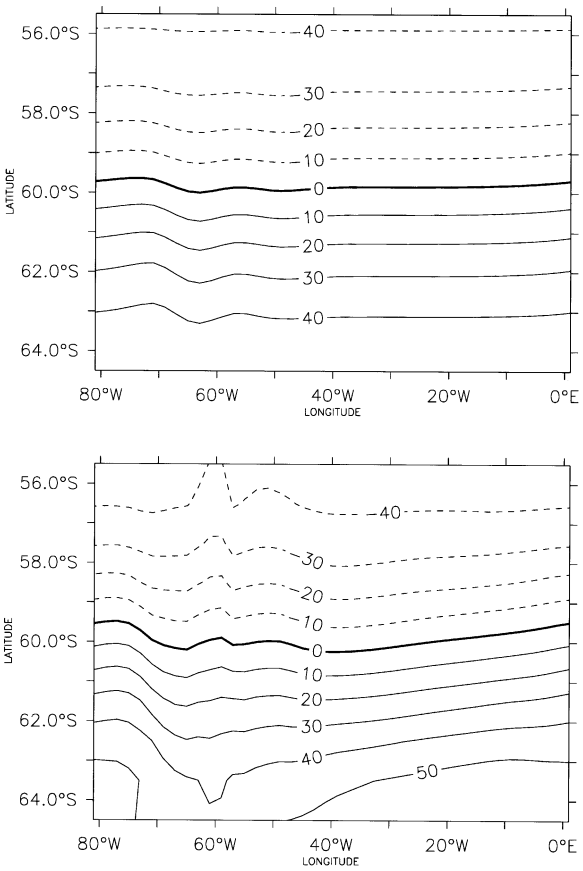

FIG. 8. Streamfunction Ψ in Sv (upper panel) and baroclinic potential energy χ/f_0 in Sv (lower panel) for the configuration C2a (thermohaline and wind forcing are both applied; see Table 1). f_0 is the Coriolis parameter at a central latitude (60°S).

(see middle panel of Fig. 12); thus some contribution of the deep transport to the total transport is indicated in the lower panel of Fig. 12, but it is still less than 25% in most of the areas. In regions, where the depth-integrated transport is not across but mostly along geostrophic contours, the above criterion does not apply and the deep transport can become quite strong. This is the case, for example, in the Weddell and Ross Seas as well as in the vicinity of the Kerguelen Plateau.

We selected two cross sections (one in the Drake Passage region and one between Tasmania and Antarctica) where the ACC has to cross geostrophic contours and the above criterion is satisfied to a reasonable degree. These selected cross sections are indicated in the Figs. 1 and 12 by lines of + marks. The cross sections are located at 146°E and 75°W. The transports $\Delta\Psi$ across the cross sections and the estimate of these transports by (13) are compared in Table 3 and Fig. 10, while Fig. 11 shows a scatterplot of (11). Several results are worth noting: (i) the transport across the section at Tasmania is 10 to 30 Sv (Sv $\equiv 10^6$ m^3 s^{-1}) stronger than the transport through Drake Passage; (ii) the inclusion of a southern restoring zone enhances the transport by about

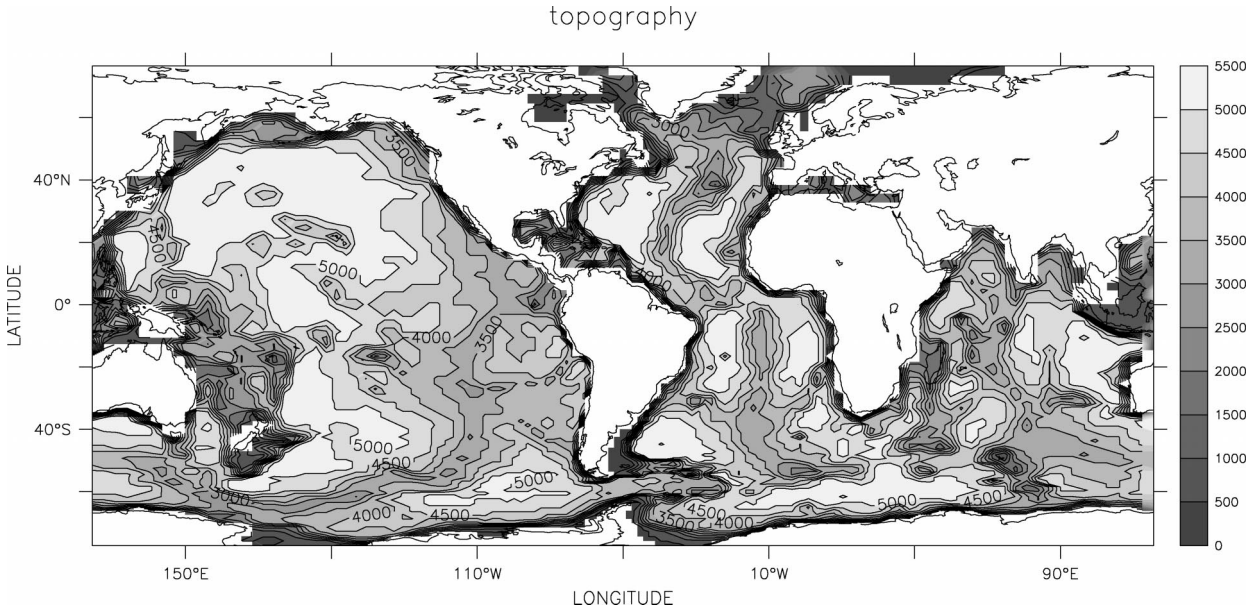

FIG. 9. Topography of the global model (contour interval is 500 m).

20 Sv, (iii) the transport across the sections decreases with increasing isopycnal thickness diffusion; and most important for our discussion, (iv) the observed transports $\Delta\Psi$ and the reconstruction of these transports by (13) agree within a range of about 10%. Thus the relation (11) proved to be a useful diagnostic within the Southern Ocean for realistic topographies as well. This is also supported by the scatterplot shown in Fig. 11.

g. Deep transport in observations and inverse models

The two cross sections above were subject of intense observational studies during the International Southern Ocean Studies (ISOS) experiment in the 1970s and early 1980s and the World Ocean Circulation Experiment (WOCE) in the 1990s. Here we try to compare the results of section 2d with observational estimates. In particular, we examine whether the proposed smallness of the contribution of the deep transport to the total transport across these two cross sections is consistent with observations.

In the ISOS experiment shipboard hydrographic sections, data from moored hydrographic instruments, pressure gauges, and current meters were combined to estimate the mean volume transport through Drake Passage (Nowlin and Whitworth 1977; Whitworth et al. 1982; Whitworth 1983; Whitworth and Peterson 1985; for reviews see Nowlin and Klinck 1986; and Rintoul et al. 2001). The agreement of the geostrophic shear derived from hydrographic sections with the vertical shear taken from direct current meter measurements was verified in Nowlin and Whitworth (1977) and Whitworth et al. (1982) for an appropriate time average of several days. A considerable variability in Drake Passage throughflow ranging from 98 to 154 Sv was observed, and the mean volume transport was estimated to be 134 $\pm$ 13 Sv (Whitworth 1983 and revised estimates in Whitworth and Peterson 1985), where the es-

TABLE 3. Summary of the configurations and results of the numerical experiments with the global model. All experiments used a 10° lat wide restoring zone near the northern boundary. In the experiments G4 to G6 a restoring zone with a latitudinal extent of 7° was also added in the south. Different values for the isopycnal thickness diffusion coefficient A_{iso} were used. The resulting depth integrated transports $\Delta\Psi$ through Drake Passage and across the section between Tasmania and Antarctica (see Fig. 12) are shown and compared with estimates from the density distribution with (13).

			Tasmania		Drake Passage	
Expt	Restoring zones	A_{iso} ($m^2\ s^{-1}$)	$\Delta\Psi$ (Sv)	Estimate (Sv)	$\Delta\Psi$ (Sv)	Estimate (Sv)
G1	Northern only	0.1×10^3	189.7	171.6	163.9	148.8
G2	Northern only	0.5×10^2	151.1	152.0	131.2	128.9
G3	Northern only	1.0×10^3	118.8	131.5	104.8	106.7
G4	Northern and southern	0.1×10^3	214.3	198.1	182.2	169.1
G5	Northern and southern	0.5×10^3	162.1	175.2	153.8	152.0
G6	Northern and southern	1.0×10^3	140.5	159.7	132.4	134.9

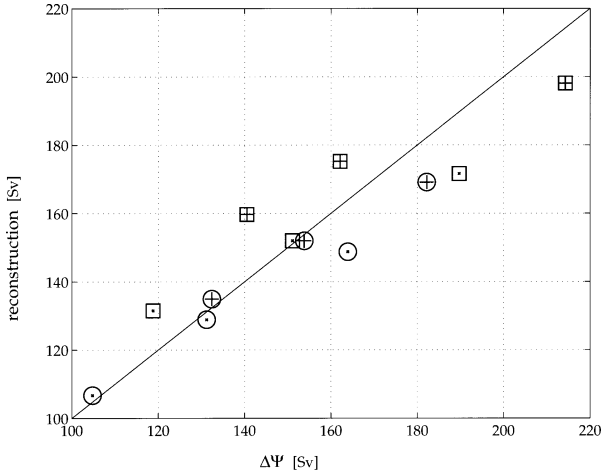

FIG. 10. Comparison of the depth integrated transports $\Delta\Psi$ through Drake Passage (marked by circles) and across the section between Tasmania and Antarctica (marked by squares) obtained from the model runs with estimates of the depth integrated transport derived from (13). The experiments with a restoring zone at the northern and the southern boundary of the model domain are labeled by ''+''. In the case of exact correspondence of $\Delta\Psi$ and the reconstruction by (13) all marks would be on the straight solid line. The observed transport $\Delta\Psi$ and the reconstruction of this transport agree within a range of about 10%.

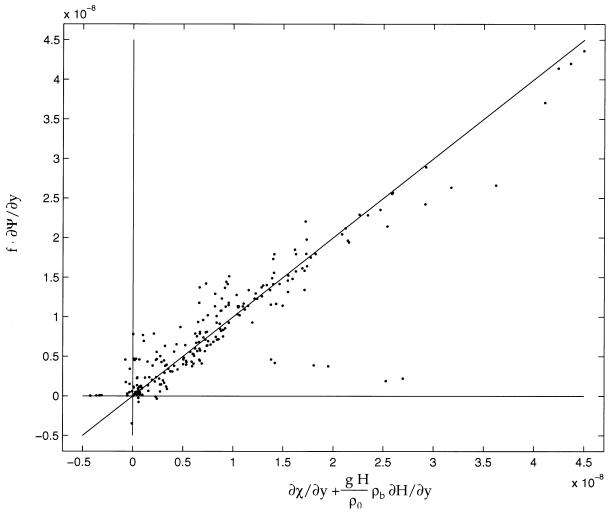

FIG. 11. Scatterplot of (11) for the six experiments with the global model, evaluated at the two meridional cross sections (one near Drake Passage and one between Tasmania and Antarctica) described in the text. The six outliners to the right of the diagonal line (one for each experiment) do all belong to the same grid point, located just south of Tasmania. There, the shear flow is not close to being zonal and is more like following f/H^{α} contours with a negative α.

timates for the mean transport above the reference level of 2500 m, above and relative to the reference level, below the reference level, and below and relative to the reference level are 125, 87, 9.1, and −6.7 Sv, respectively. Thus 70% of the transport above 2500 m is found in the baroclinic shear (above and relative to 2500 m). In the context of this paper, the transport relative to the bottom layer is more relevant than the transport relative to the 2500-m level, but Whitworth (1983) and Whitworth and Peterson (1985) did not provide values for this transport. However, since part of the flow at 2500 m is already a baroclinic flow relative to the bottom layer, we expect the contribution of the transport relative to the bottom layer to the total transport to be somewhat greater than the comparison on the basis of the 2500-m reference level suggests.

The WOCE hydrographic repeat section SR3 is very similar to the cross section between Tasmania and Antarctica considered in the global model above. Rintoul and Bullister (1999) and Rintoul and Sokolov (2001) estimated the geostrophic transport across this section relative to the deepest common depth at each hydrographic station pair, and obtained transport values between 146 and 181 Sv. In addition, Rintoul and Bullister (1999) and Rintoul and Sokolov (2001) provided estimates for the geostrophic transport relative to a deep ''best guess'' reference level consistent with water mass properties and float trajectories. This best-guess reference level approximates a near-bottom reference level, except at the southern end of the hydrographic section where the best guess reference level allows for a westward flow above the upper continental slope of Antarctica. The transport relative to this best-guess reference level ranges from 135 to 158 Sv with a mean value of 147 ± 10 Sv. With an inverse model and applying the least squares dynamically constrained optimization technique to hydrographic, wind stress, and current meter data Yaremchuk et al. (2001) estimated the total transport across SR3 to range from 137 ± 29 to 161 ± 30 Sv with a mean of 151 ± 50 Sv. Comparing the estimates of the total transport by Yaremchuk et al. (2001) with the transport relative to the best-guess reference level estimated by Rintoul and Sokolov (2001), the estimates agree within the limits of the error bars. The transport relative to the deepest common depth reference level, which can be considered as an approximation of the shear transport relative to the bottom (see section 2d), tends to overestimate the total transport by around 10%.

By applying (13) to the Levitus (1982) dataset one obtains 158.6 Sv for the Drake Passage transport and 171.8 Sv for the transport across the Tasmania cross section. These estimates lie about 18% above the estimate by Whitworth (1983) and Whitworth and Peterson (1985) for the Drake Passage transport and 14% above the estimate by Yaremchuk et al. (2001) for the transport across SR3. Some of these differences can be explained, for example, by the westward flow at the Antarctic continental slope where the current is more parallel than across the geostrophic contours. Apart from this, the observations in principle confirm the assumption that the deep transport ascribed to the bottom flow makes a negligible contribution to the total transport at the two cross sections considered. This is also consistent with the inverse box model of Macdonald (1998). Rintoul et

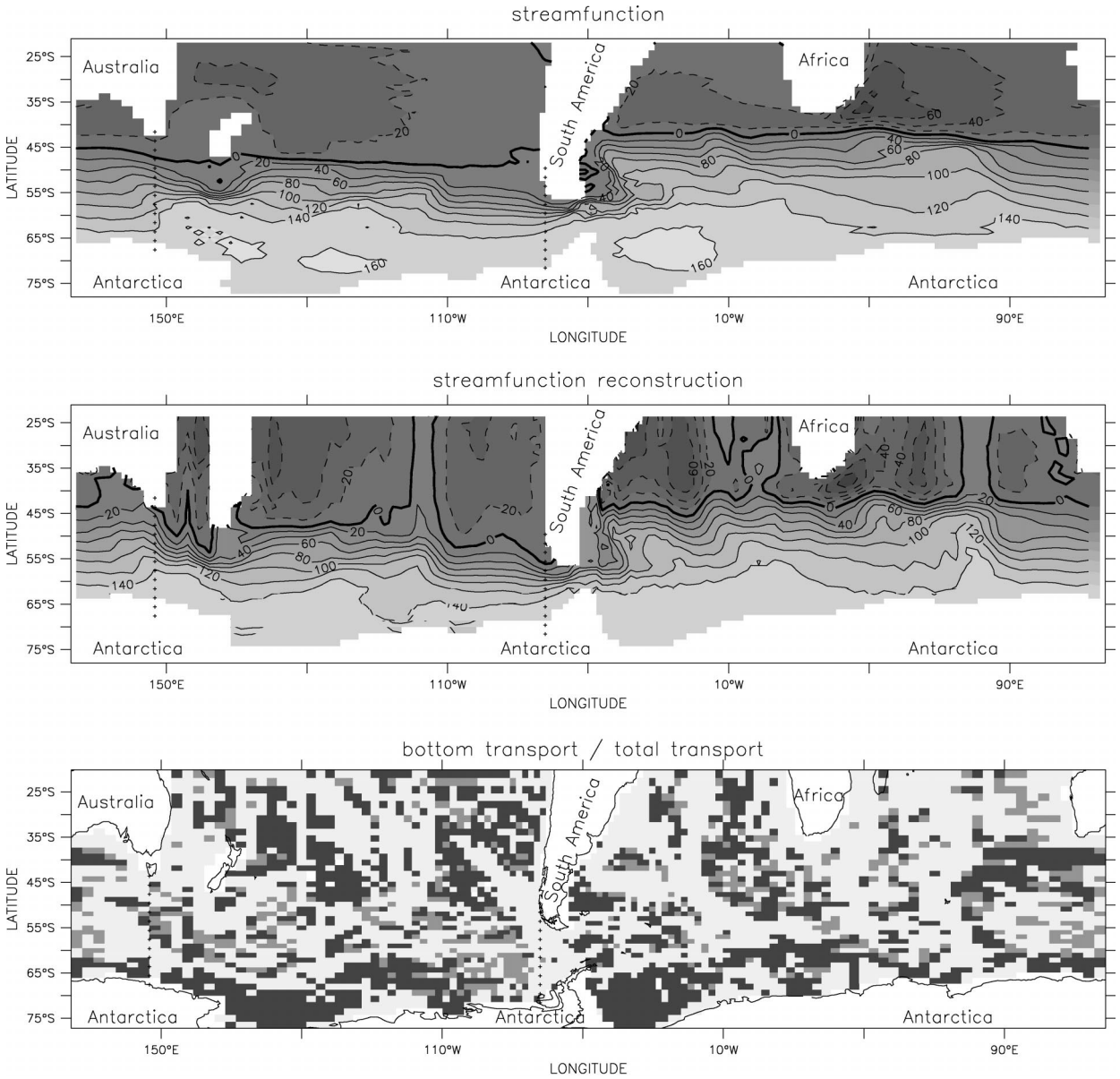

FIG. 12. Results of the experiment G5 (see Table 3): (upper panel) streamfunction Ψ in Sv, (middle panel) reconstruction of the streamfunction with (13), and (lower panel) ratio of the magnitude of the bottom transport $\mathbf{U}_{\text{deep}}$ [see (4)] and the magnitude of the total transport $\mathbf{U}$. In the light shaded areas this ratio is less than 10%, in the middle gray shaded areas it is between 10% and 25%, and in the dark shaded areas more than 25%. In all panels above, as well as in Fig. 1, the sections chosen for the comparison of the transports $\Delta\Psi$ with the estimates of these transports with (13) are marked with lines of +. These sections are located between Tasmania (Australia) and Antarctica at 146°E and across Drake Passage at 75°W.

al. (2001) questioned whether the inverse models of Yaremchuk et al. (2001) and Macdonald (1998) can really provide conclusive arguments for a small contribution of the deep transport to the total transport, since the inverse models start with a first guess of zero bottom flow. Losch (2000) and Losch and Schröter (2002, manuscript submitted to *J. Phys. Oceanogr.,* hereafter LOSC) assimilated altimeter data into the model of Yaremchuk et al. (2001) to improve the estimate of the barotropic transport across SR3. However, obtaining a total volume transport of 210 $\pm$ 27 Sv and a structure of the flow, which they argued to be inconsistent with hydrography, Losch (2000) and LOSC rejected this result and considered this as an indication that the published errors of the EGM96 geoid model could be too small. To conclude this subsection: the assumption of a small contribution of the deep transport to the total transport through Drake Passage and across the SR3

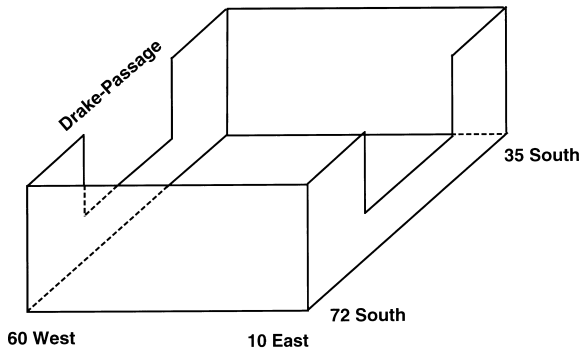

FIG. 13. Geometry of the periodically connected rectangular basin.

section, for which some dynamical arguments were provided in section 2d, can be considered to be consistent with the observations currently available.

3. The thermodynamic balance

So far, only the dynamic balance has been considered, and the approximate balances (2), (11), and (12) were suggested. According to these approximate balances, the circumpolar channel transport is to leading order determined by the density field summarized in χ. A direct influence of the wind stress field $\boldsymbol{\tau}$ on the transport is not seen in (2), (11), or (12). The wind stress does not affect the circumpolar transport through a vertical frictional flux of zonal momentum. However, the wind may influence the circumpolar transport in a more indirect way through its effect on the density field. Such effects were investigated by, for example, Cai and Baines (1996) and Gnanadesikan and Hallberg (2000) and are addressed in this section.

a. A periodically connected rectangular basin

To study the effects of wind forcing on the density field, a further idealized numerical model was used (Fig. 13). The chosen geometry is similar to the one used by Gill and Bryan (1971), but is restricted to the latitudes south of 35°S with solid walls at the boundaries. This geometry allows Ekman pumping and water mass conversion to occur north and south of a circumpolar connection.

The horizontal resolution is $2° \times 2°$ and the model contains 15 unequally spaced levels with a resolution varying from 30 m at the surface to 730 m at the bottom at depth 5700 m. The circumpolar connection is 3000 m deep and extends from 62° to 42°S. Subgrid-scale mixing is parameterized with a turbulent viscosity of 2×10^5 m^2 s^{-1} in the horizontal and 10^{-3} m^2 s^{-1} in the vertical and a turbulent diffusivity of 2×10^3 m^2 s^{-1} in the horizontal and 10^{-4} m^2 s^{-1} in the vertical. Again, the distorted physics technique of Bryan (1984) was applied to accelerate the convergence to an approximate steady state. Surface temperatures and salinities are restored to zonal mean values based on averages of Levitus (1982) and a zonally constant zonal wind stress is applied using zonal averages of Hellerman and Rosenstein (1983). In the experiments, the wind stress was varied by multiplication with a factor of -1, $-1/2$, 0, 1/2, or 1. The model was restored to different sea surface temperatures and salinities, and the sensitivity to the parameterization of turbulent diffusion was investigated. Starting with homogeneous water masses at rest the model was integrated for 2000 years to a near-steady state.

A comparison of the streamfunction Ψ with the baroclinic potential energy χ/f_0 for the experiments with positive wind stress, zero wind stress, and negative wind stress in Figs. 14, 15, and 16 by and large confirms the balance (11) for the periodically connected rectangular basin. With positive wind stress, a channel transport of 185 Sv is obtained, while the potential energy integral yields about 160 Sv, estimated at the eastern side of the rectangular basin or 180 Sv estimated at its western side. The density field is characterized by a very weak stratification at high latitudes and a pronounced permanent pycnocline in middle latitudes. In the latitude band of the circumpolar connection the model produces a strong meridional density gradient in the upper 2 km of the water column. The zonally averaged transport features a pronounced southern sinking cell and a Deacon cell where around 4 Sv are carried southward below the sill depth of the passage. The Deacon cell vanishes with zero wind stress (Fig. 15), and the southern sinking cell is weakened. The pycnocline and the meridional density gradient are much weaker. Correspondingly, we find a much weaker contrast in the potential energy integral that is, again, in good agreement with the streamfunction for the vertically integrated flow.

The negative wind stress case (Fig. 16) reveals a strongly nonlinear response of the model to the wind forcing. A westward transport, however, establishes that the strength is only around 10 Sv, far away from the 20 times larger response to positive wind forcing. In the interior of the rectangular basin, where the topography is flat, the fields of the streamfunctions and the baroclinic potential energy deviate significantly. While the streamfunction shows a closed gyre, as would be expected from Sverdrup theory, the contours of the baroclinic potential energy are mainly zonal. However, at the topographic barrier located at the circumpolar connection, where the geostrophic contours are blocked and the arguments of the preceding section should apply, good agreement between streamfunction and potential energy integral can be found. The reversal in the meridional gradient of the potential energy integral is related to a depression of isopycnals in the latitude band of the circumpolar connection. This depression in turn is related to the two upwelling branches of the meridional overturning circulation at around 60°S and north of 45°S. The influence of the wind forcing, the meridional overturning circulation, and the parameter values

of the turbulent diffusivity on the deep stratification and on the channel transport will be discussed to some detail in following subsections.

b. Ekman transport and deep stratification

The experiments with the periodically connected rectangular basin showed a relation between the distribution of the zonally averaged potential density $\overline{\sigma}$ and the meridional overturning streamfunction Φ in addition to the close correspondence of the streamfunction Ψ and the baroclinic potential energy χ that was elaborated before.

1) Ekman convergence (divergence) north of the circumpolar connections leads to downwelling (upwelling) there. The vertical extent of this motion is reflected in a zonally integrated sense in the overturning streamfunction Φ. The northward (southward) Ekman transport connected with the eastward, that is, positive (westward, i.e., negative) winds in the latitudes of the circumpolar connection must be balanced by a southward (northward) return flow below the depth of the circumpolar connection of 3000 m. Thus the zonally integrated meridional overturning streamfunction Φ indicates a deep reaching downwelling (upwelling) branch north of the circumpolar connection.
2) The downwelling (upwelling) leads to a deepening (shallowing) of the pycnocline to the north of the circumpolar connection. This in turn enhances (weakens) the meridional gradient of the baroclinic potential energy χ.
3) According to our discussion of section 2, an enhanced (weakened) meridional gradient of the baroclinic potential energy χ must result in a stronger (weaker) channel transport $\Delta\Psi$.

In a steady state, the balance of the zonally averaged density field $\overline{\sigma}$ is written as

$$J(\Phi, \overline{\sigma}) = A_v\frac{\partial^2\overline{\sigma}}{\partial z^2} + A_h\frac{\partial^2\overline{\sigma}}{\partial y^2} - \left(\frac{\partial\overline{v^*\sigma^*}}{\partial y} + \frac{\partial\overline{w^*\sigma^*}}{\partial z}\right), \tag{14}$$

where the overbar denote zonal mean, asterisk quantities the deviations from the zonal mean (e.g., $\sigma^* = \sigma - \overline{\sigma}$), and subgrid mixing is simply represented by turbulent diffusion. In the experiments with the rectangular basin with circumpolar connection, we found that the standing eddy components are irrelevant below a depth of, roughly, 500 m. Thus, in the subsequent discussion of the thermodynamic balance, these standing eddy components are omitted and we consider the proposed physical mechanism as appropriate to the model configuration used for the experiments. A more detailed discussion of the eddy induced transports will follow in section 3e.

c. An idealized analytical model

The above mechanism is here summarized in a simple analytical model of the circumpolar current in the periodically connected rectangular basin. With this simple model we attempt to reproduce the qualitative dependence of the channel transport on the thermohaline and wind forcing as well as on the parameter values of turbulent diffusion. A schematic diagram of the model is given in Fig. 17.

At high southern latitude the stratification is weak. For our purposes, it is sufficient to assume a homogeneous density ρ_0 south of the circumpolar connection. Below the depth of the gap, this water can geostrophically spread to the north and is supposed to fill the whole abyss of the rectangular basin. Assume that Φ has the overall structure of the Deacon cell, revealed in the experiments, with an amplitude set by the Ekman transport T_{Ek}. Then $\overline{w} \approx -T_{\mathrm{Ek}}/L_1$ in the northern downwelling branch, and one can approximate (14) by

$$-\frac{T_{\mathrm{Ek}}}{L_1}\frac{\partial\rho}{\partial z} = A_v\frac{\partial^2\rho}{\partial z^2} + \frac{A_h}{L_2^2}(\rho_0 - \rho)$$

$$\Rightarrow \frac{\partial^2\rho}{\partial z^2} + \left(\frac{1}{L_v}\right)\frac{\partial\rho}{\partial z} + \left(\frac{1}{L_v^*}\right)^2(\rho_0 - \rho) = 0, \tag{15}$$

where L_1 and L_2 are horizontal length scales of the Ekman pumping and lateral turbulent diffusion respectively, $L_v = (A_v/T_{\mathrm{Ek}})L_1$ is a vertical Munk scale (Munk 1966), $L_v^* = \sqrt{(A_v/A_h)}L_2$ a vertical scale of turbulent diffusion, and $\rho(z)$ is the northern density profile; A_h and A_v are the lateral and vertical turbulent diffusivities. The horizontal diffusion is approximated by the horizontal density difference. With setting $\rho = \rho_+$ at the surface ($z = 0$) and $\rho \approx \rho_0$ in the deep ocean ($z = -D$), Eq. (15) is solved by

$$\rho = \rho_0 + (\rho_+ - \rho_0)e^{z/\delta} \tag{16}$$

with an inverse scale depth

$$\left(\frac{1}{\delta}\right) = \sqrt{\left(\frac{1}{L_v^*}\right)^2 + \left(\frac{1}{2L_v}\right)^2} - \left(\frac{1}{2L_v}\right). \tag{17}$$

Note, since δ is small for almost all experiments, we omitted the second root of (17) for simplicity of discussion.

We estimate the channel transport $\Delta\Psi$ by $\Delta\chi/f_0$. Integrating the potential energy over the depth D of the gap, a simple equation is obtained:

$$\Delta\Psi \approx \frac{1}{f_0}\left(\frac{g}{\rho_0}\int_{-D}^{0} z\rho\, dz - \frac{g}{\rho_0}\int_{-D}^{0} z\rho_0\, dz\right)$$

$$= -\frac{g}{f_0}\frac{\rho_0 - \rho_+}{\rho_0}\delta^2\left(1 - \left[1 + \frac{D}{\delta}\right]e^{-D/\delta}\right), \tag{18}$$

which predicts the channel transport $\Delta\Psi$ from the wind forcing T_{Ek}, the prescribed density difference $(\rho_0 - \rho_+)$,

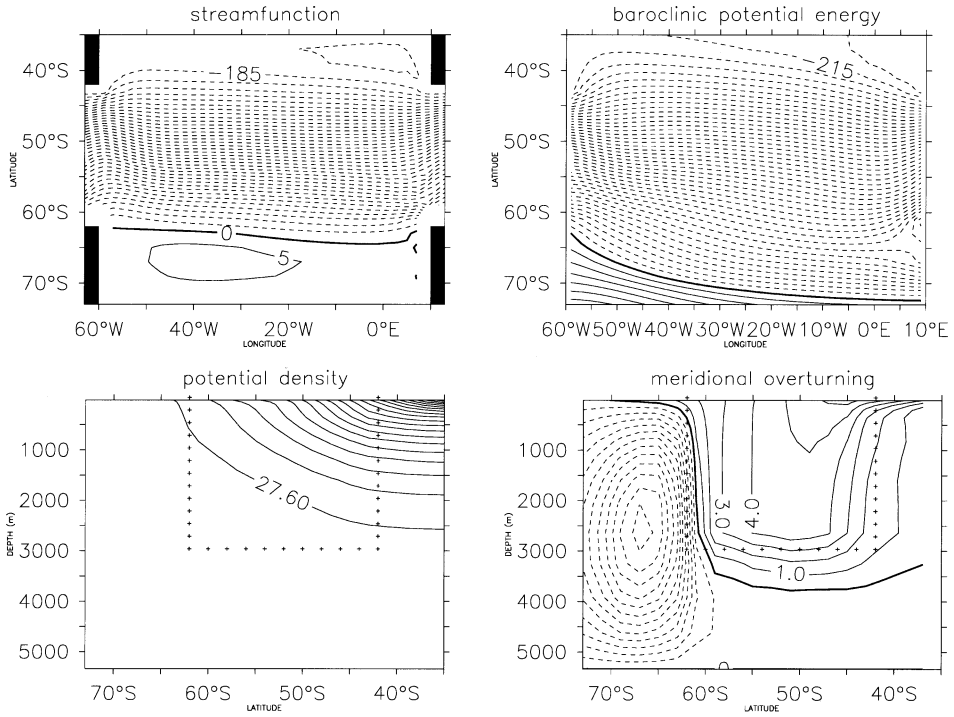

FIG. 14. *Positive wind case*: streamfunction Ψ in Sv, baroclinic potential energy χ/f_0 in Sv, zonally averaged potential density $\overline{\sigma}$, and meridional overturning Φ in Sv. The lines marked by crosses indicate the position of the circumpolar connection, and f_0 is the Coriolis parameter at 50°S.

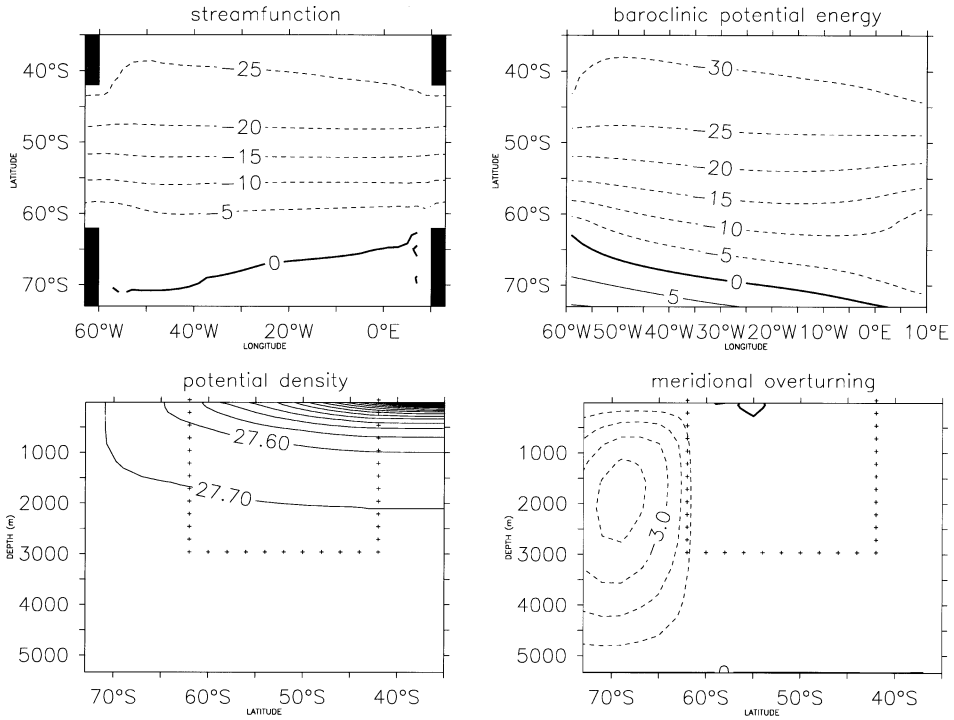

FIG. 15. *Zero wind case*: streamfunction Ψ in Sv, baroclinic potential energy χ/f_0 in Sv, zonally averaged potential density $\overline{\sigma}$, and meridional overturning Φ in Sv. The lines marked by crosses indicate the position of the circumpolar connection, and f_0 is the Coriolis parameter at 50°S.

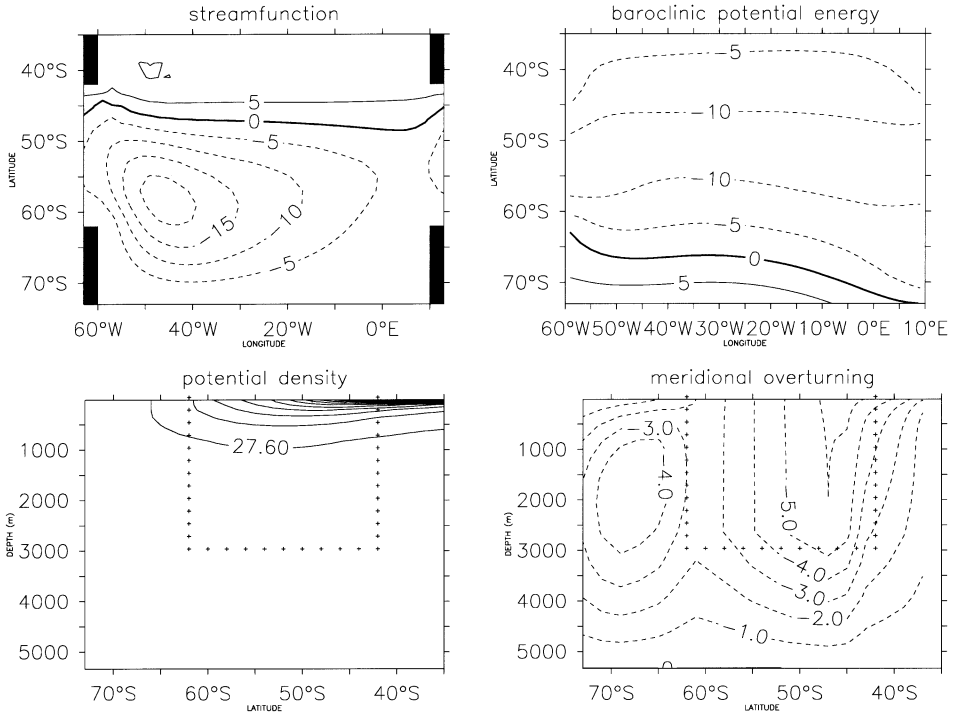

FIG. 16. *Negative wind case*: streamfunction Ψ in Sv, baroclinic potential energy χ/f_0 in Sv, zonally averaged potential density $\overline{\sigma}$, and meridional overturning Φ in Sv. The lines marked by crosses indicate the position of the circumpolar connection, and f_0 is the Coriolis parameter at 50°S.

and the parameters A_h, A_v, L_1, and L_2. The Ekman transport T_{Ek} and the parameters of the turbulent diffusion A_h, A_v are specified in the configurations of numerical experiments, but the choice of ρ_0, ρ_+, L_1, and L_2 is somewhat ambiguous. The length scale L_1 must represent the meridional extent of the downwelling (upwelling) region north of the circumpolar connection, and L_2 should approximate the horizontal length scale of the density gradient. Both may be different for the different numerical experiments. This also holds for the densities ρ_0 and ρ_+ of the densest and lightest water available. Within the range of reasonable parameter values, we chose the parameters ρ_0, ρ_+, L_1, and L_2 (one set of parameters which is used for all experiments) to obtain a good fit of (18) to all numerical results. The parameters used are listed in Table 4.

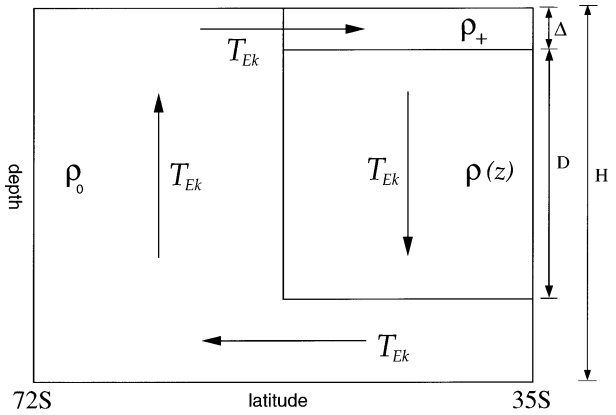

FIG. 17. Schematic diagram of the idealized analytical model. At high southern latitudes and below the depth of the circumpolar connection (D) dense water of the density ρ_0 is assumed. North of the circumpolar connection and advective diffusive balance for the potential density is used to obtain $\rho(z)$ as a function of the depth z. Due to Ekman pumping north of the gap, the densities are advected vertically downward with T_{Ek}/L_1, where L_1 is a horizontal length scale of the Ekman pumping. The surface density north of the gap is ρ_+.

The upper-left panel of Fig. 18 compares the channel transport as a function of the applied wind stress, as given by (18), with the results obtained from the numerical experiments. The agreement of the simple model with the numerical experiment is rather good; however, concerning the quantitative agreement, some scepticism is appropriate. One noticeable qualitative differ-

TABLE 4. Parameters used in (18).

g	9.81 kgm s^{-2}
f_0	$-1.117 \cdot 10^{-4}$ l s^{-1}
A_h	$2 \cdot 10^3$ m^2 s^{-1}
A_v	10^{-4} m^2 s^{-1}
ρ_0	1027.7 kg m^{-3}
ρ_+	1025.7 kg m^{-3}
τ^x	0.118 N m^{-2}
D	3000 m
L_1	1300 km
L_2	1700 km

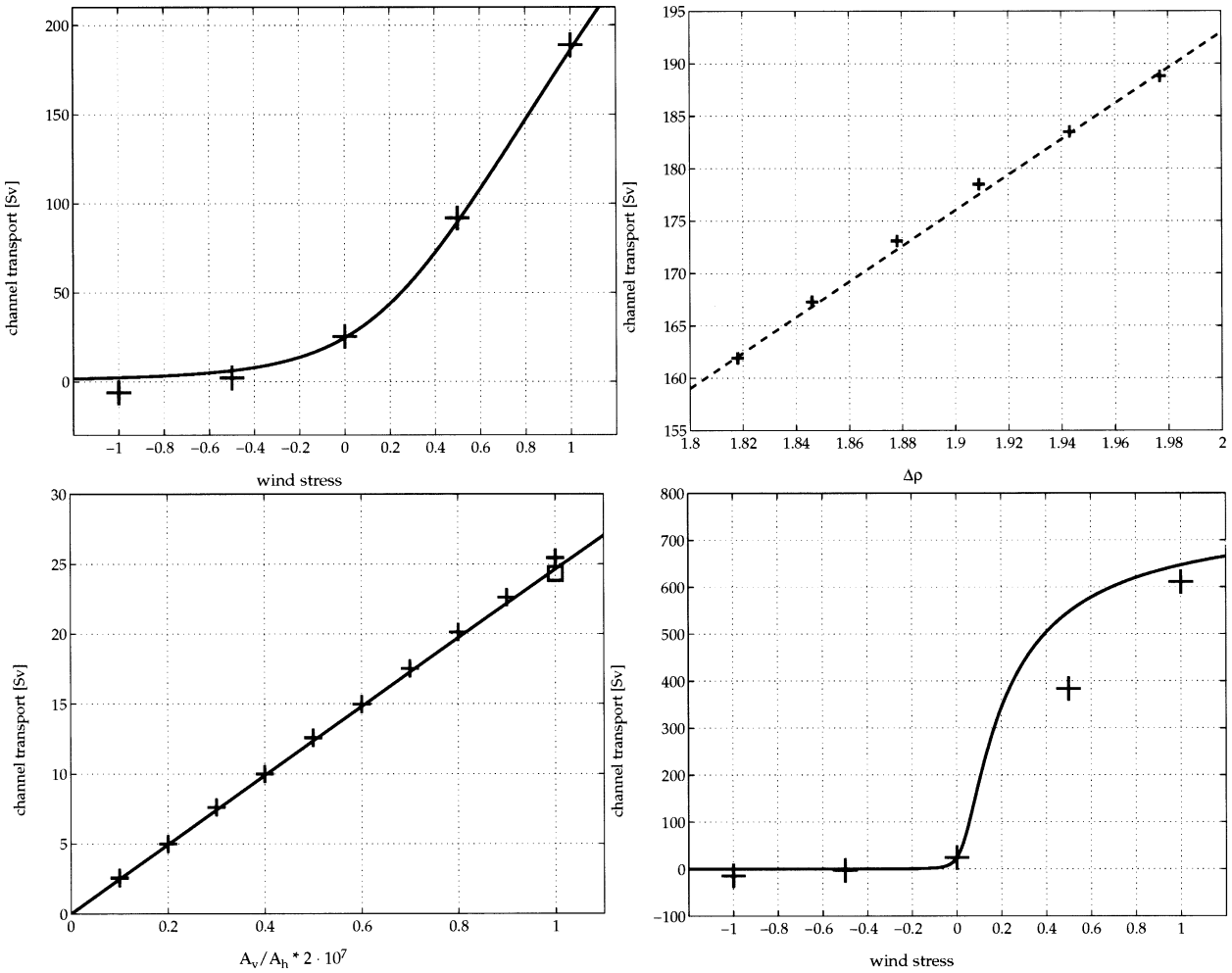

FIG. 18. (upper-left panel) Channel transport $\Delta\Psi$ in Sv vs wind stress for the periodically connected rectangular basin. The crosses indicate numerical model results and the solid line the relation (18). (upper right panel) $\Delta\Psi$ vs thermohaline surface forcing $\Delta\rho$ in kg m^{-3} for experiments with positive wind stress. The dashed line compares the numerical results with a linear relationship. (lower-left panel) $\Delta\Psi$ vs the ratio A_v/A_h of the vertical and lateral diffusivities in the limit of zero wind stress. The crosses represent experiments with a constant lateral diffusivity of $A_h = 2.10^3$ m^2 s^{-1} and vertical diffusivities of $A_v = (1 \cdots 10) \times 10^{-5}$ m^2 s^{-1}, the rectangle signifies an experiments with $A_v = 10^{-5}$ m^2 s^{-1} and $A_h = 2 \times 10^2$ m^2 s^{-1}, and the solid line the relation (18). (lower-right panel) $\Delta\Psi$ vs wind stress for the experiments with reduced vertical and horizontal turbulent diffusivities ($A_v = 10^{-5}$ m^2 s^{-1} and $A_h = 2 \times 10^2$ m^2 s^{-1}). All other parameters of (18) are taken from Table 4.

ence is the slight westward transport in the numerical experiment with negative wind stress, while (18) implies eastward transports for any wind stress. In the negative wind stress case of the numerical experiments, the pycnocline north of the circumpolar connection is depressed and there the meridional density gradient is reversed (see Fig. 16). Within the simple analytical model, a reversal of density gradients is impossible and thus a negative transport cannot be obtained.

The relation (18) implies a linear dependence of the channel transport $\Delta\Psi$ on the imposed density difference $\Delta\rho = \rho_0 - \rho_+$. We conducted various experiments, changing the thermohaline forcing but keeping the other parameters constant. The upper-right panel of Fig. 18 displays the results for the experiments with positive wind stress. The crosses lie almost on a straight line, but a closer look reveals a slightly concave shape.

d. The influence of diffusivity

In the limit of zero wind stress (18) becomes

$$\lim_{\tau \to 0} (\Delta\Psi) \approx -\frac{g}{f_0} \frac{\rho_0 - \rho_+}{\rho_0} \frac{A_v}{A_h} L_2^2 \qquad (19)$$

and implies a linear dependence of the channel transport on the ratio A_v/A_h of the vertical and lateral diffusivities. We conducted various experiments with different diffusivities A_v and A_h. The results of experiments with zero wind stress are displayed in the lower-left panel of Fig. 18. Consistent with (19) the numerical experiments

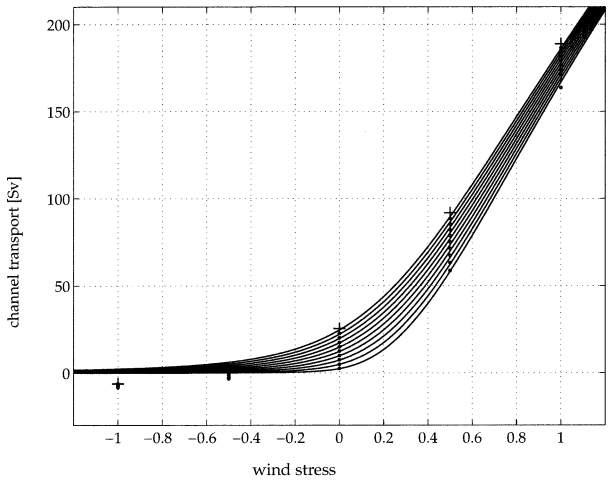

FIG. 19. Channel transport vs wind stress for experiments with the rectangular basin, using different vertical diffusivities A_v. The crosses indicate the numerical results for $A_v = 10 \times 10^{-5}$ m^2 s^{-1}, the dots the numerical results for $A_v = (1 \cdots 9) \times 10^{-5}$ m^2 s^{-1}, and the solid lines relation (18). Besides A_v, all parameters are chosen as listed in Table 4.

show a linear relationship between $\Delta\Psi$ and A_v/A_h. The results of the numerical experiments, varying the wind stress as well as the vertical diffusivity, are shown in Fig. 19 and compared with the estimates by (18). The qualitative behavior of the numerical experiments is again well reproduced by (18). The channel transport $\Delta\Psi$ increases with an increased vertical diffusivity A_v, and the wind-induced additional transport decreases with an increase in A_v. Running the model with both the vertical and the lateral diffusivity reduced by a factor 10 (see lower-right panel of Fig. 18), the channel transport shows signs of beginning to saturate with increasing wind stress. This feature is also reproduced by (18). This effect can be explained as follows: If the water column north of the gap is already filled (from the surface down to the depth of the gap) by light water of the potential density ρ_+, a further increase in the wind stress cannot increase the meridional density gradient. Thus it cannot increase the channel transport either. However, in addition, it may be noted that in these circumstances δ can no longer be considered small, and thus, without using the second root of (17) as well, (18) is a poor fit to the model results.

In their global coarse resolution model Cai and Baines (1996) investigated the effects of increasing the vertical diffusivity by a factor of 5. Without wind stress, they observed an ACC transport increased by a factor of 3.25. Equation (19) would suggest an increase of the ACC transport by a factor of 5, but the qualitative tendency is the same. The additional ACC transport due to the wind forcing decreased by 21.8% in the Cai and Baines (1996) experiments, which is also consistent with our findings displayed in Fig. 19. The principle dependence of the ACC transport on the vertical diffusivity, as proposed by the idealized analytical model, can be further compared with the model results of Toggweiler and Samuels (1998), which are also consistent with our findings.

e. The meridional circulation in coarse and fine resolution models

In this section we discuss some effects that were neglected in the present study, that is, the effects of standing eddies on the so called Deacon cell as discussed by Döös and Webb (1994), the possible coupling of the Southern Hemisphere winds with the North Atlantic Deep Water formation as proposed by Toggweiler and Samuels (1995), and the role of the North Atlantic Deep Water on the ACC transport as found, for example, in Goodman (1998).

By considering the changes in the density field due to changes of the wind-driven Deacon cell, and by discussing the change of the Drake Passage transport due to a changed density field, we describe an indirect effect of the Southern Ocean winds on the Antarctic Circumpolar Current. As a simplification, we assume a large-scale deep downward tracer advection just north of Drake Passage to be connected with the zonally averaged overturning circulation of the Deacon cell, and state a balance of the large-scale tracer advection and the turbulent tracer diffusion. In the sections 3c and 3d, we obtained a satisfactory representation of the zonal transport with these simplifying assumptions.

Such a view of the Deacon cell, as a tracer advecting meridional cell, is criticized by Döös and Webb (1994). They analyzed the Fine Resolution Antarctic Model (FRAM) and compared the meridional transport, zonally averaged along levels of constant depth, with the meridional transport, zonally averaged along surfaces of constant potential density. While the Deacon cell was clearly reproduced with the first procedure of zonal averaging, the Deacon cell almost completely disappeared by zonal averaging along surfaces of constant potential density. Döös and Webb concluded that there is no diapycnic tracer transport connected with the Deacon cell. This is contrary to our simplifying assumption used in sections 3b and 3c.

However, by comparing the zonal mean and the standing eddy components of the zonally averaged advection operator in section 3b we found a deep downwelling of tracers to be connected with the large-scale Ekman convergence in the northern part of the Deacon cell. Thus our simple advective–diffusive balance does apply to our coarse-resolution model with the specified geometry. A Deacon cell with a deep downwelling northern branch is also present in many other coarse-resolution models, and, though it may be an unrealistic feature, it seems to be at least a feature of coarse-resolution models.

Danabasoglu and McWilliams (1995) investigated the effects of the Gent and McWilliams (1990)/Gent et al. (1995) parameterization in a coarse-resolution global

domain model. Beside other important effects, they observed that the Deacon cell is eliminated as a tracer transport agent, and they recommended use of the Gent and McWilliams (1990) parameterization in coarse-resolution global ocean models. In the Gent and McWilliams (1990) parameterization the Eulerian mean transport velocity of the advection operator is replaced by an effective transport velocity, which is the sum of the Eulerian mean and an eddy-induced transport velocity. In Danabasoglu and McWilliams (1995) the Deacon cell is present in the Eulerian mean transport velocity, but is compensated by the additional eddy-induced tracer advection, and vanishes in the effective transport velocity. The eddy-induced vertical tracer transport velocity of Gent and McWilliams (1990)/Gent et al. (1995) is parameterized using the curvature of the isopycnals and effectively restores the isopycnals toward plane and uncurved surfaces. While, within the northern branch of the Deacon cell, the Eulerian mean transport velocity tends to displace the isopycnals downward, the eddy-induced transport velocity tends to restore the isopycnals; in the state investigated by Danabasoglu and McWilliams (1995) both velocities do balance each other.

Instead of using the advective–diffusive balance of section 3c, one could use the Gent and McWilliams (1990)/Gent et al. (1995) parameterization and state a balance of the Eulerian mean and the eddy-induced transport velocity. Though the physical description of the small-scale details is rather different, the broad large-scale consequences would be very similar. The indirect effect of the Southern Ocean winds on the Drake Passage transport through a change of the density field can be reproduced with the Gent and McWilliams (1990)/Gent et al. (1995) parameterization. The numerical experiments of Gent et al. (2001) support this view.

However, since the Gent and McWilliams (1990) parameterization only accounts for the transient/small-scale eddies and not the large-scale/standing eddies, the point made by Döös and Webb (1994) remains relevant. A thorough analysis of the meridional circulation in terms of Eulerian circulation, transient eddy, standing eddy, and residual circulation can be found in Olbers and Ivchenko (2001), where the formalism of the transformed Eulerian mean (TEM) is applied to the eddy-resolving global ocean model Parallel Ocean Program (POP: Smith et al. 1992; Maltrud et al. 1998). The standing eddies generate an intensive cell in the Southern Ocean of POP that is concentrated in the upper 600 m. A narrow, fairly deep reaching circulation in the Drake Passage belt is induced by the transient eddies. Thus, while in the upper ocean the standing eddy contribution dominates the circulation, the deeper parts of the Deacon cell are compensated by a circulation induced by transient eddies. Thus, in the deep ocean the Gent and McWilliams (1990) parameterization may be considered as an appropriate representation of eddy effects, and there the elimination of the Deacon cell with the Gent and McWilliams (1990) parameterization as observed by Danabasoglu and McWilliams (1995) is consistent with the findings of Olbers and Ivchenko (2001).

Toggweiler and Samuels (1995) proposed an alternative route for the return flow of the water masses driven northward by the Southern Ocean winds in the ACC belt. Instead of assuming deep downwelling just north of Drake Passage (as it is done in this paper), Toggweiler and Samuels (1995) suggest a link of the Southern Ocean winds with the North Atlantic overturning circulation (''Drake Passage Effect''). Observing a dependence of the North Atlantic meridional overturning on the Southern Hemisphere winds in their model experiments, they suggest that the water masses, pushed northward by the Ekman drift in the latitudes of Drake Passage, continue to flow northward and join the North Atlantic overturning circulation. The northward Ekman transport in the latitudes of Drake Passage is then compensated by a southward flow of North Atlantic Deep Water.

According to Toggweiler and Samuels (1995), a wind-induced deep downwelling in the northern branch of the Deacon cell should only occur if the North Atlantic overturning is prohibited or limited in some way. In our idealized geometry of the periodically connected rectangular basin, we prohibit the North Atlantic overturning by an artificial solid wall at 35°S. Thus the ''Drake Passage Effect'' can a priori not be observed in our periodically connected rectangular basin, and we might have omitted an important effect.

In McDermott (1996), Goodman (1998), and Gnanadesikan and Hallberg (2000) a mechanism is revealed, through which the Drake Passage effect could have an impact on the Antarctic Circumpolar Current. Gnanadesikan (1999) offers a simple predictive model for the pycnocline depth, where he assumes a balance of (i) vertical diffusion within the pycnocline, (ii) upwelling through the pycnocline in low latitudes, (iii) the conversion of light to dense water associated with the formation of North Atlantic Deep Water, (iv) Southern Ocean winds, and (v) Southern Ocean eddies. Concentrating on the processes (iii) and (iv), Gnanadesikan and Hallberg (2000) argue that the Southern Ocean winds to have two effects on the density structure.

1) By increasing (decreasing) the Southern Ocean winds, more (less) deep water rises in the Southern Ocean, which leads to a deepening (shallowing) of the pycnocline.
2) In order to balance the increased (decreased) wind driven upwelling in the Southern Ocean, the overturning circulation in the North Atlantic must strengthen (weaken). Thus the northward heat transport is increased (decreased) and the North Atlantic Deep Water is warmed (cooled).

Both effects lead to an increased thermal wind shear across Drake Passage and thus an increased ACC trans-

port, when the Southern Ocean winds strengthen, and a decreased thermal wind shear and ACC transport, when the Southern Ocean winds weaken.

Rahmstorf and England (1997) critically examined the Drake Passage effect by including a simple atmospheric feedback model to their OGCM. The atmospheric feedback tends to weaken the link between the Southern Ocean winds and the North Atlantic overturning circulation. Only one-third of the water mass driven northward by the Ekman drift in the ACC belt is returned through overturning in the North Atlantic. In the experiments of Rahmstorf and England (1997) two-thirds of these waters sink just north of Drake Passage. This implies, that the density field in the vicinity of Drake Passage is largely determined by local processes very similar to the processes assumed in this paper. Local processes influencing the density field north of Drake Passage are also realized in Gnanadesikan (1999) by the parameterization of the Southern Ocean eddies with Gent and McWilliams (1990).

Though a deep downwelling northern branch of the Deacon cell might be a somewhat unrealistic view of the processes occurring in the ocean, the principal effects described by the analytical model of section 3c can be expected to be (to some extent) relevant in the real ocean as well.

4. Summary and conclusions

Two main conclusions are put forward in this paper.

1) In the case of a circumpolar channel with blocked geostrophic contours, the circumpolar transport is to leading order determined by the meridional gradient of the baroclinic potential energy. Balances (11) and (13) express this statement, and we propose these balances as useful diagnostics for the Southern Ocean. No direct effect of the wind stress can be found in (11), and we conclude that the circumpolar current is not directly driven by wind stress.
2) Indirect effects of the Southern Ocean winds on the ACC transport, as suggested by Cai and Baines (1996), Gnanadesikan and Hallberg (2000), and Gent et al. (2001), are supported by this study. The wind stress has a pronounced influence on the circumpolar transport through its effects on the density field. A simplified analytical model is developed to investigate these effects. With this model we are able to reproduce the qualitative dependence of the channel transport on the wind forcing, thermohaline forcing, and the parameters of turbulent diffusion, as observed in the numerical model runs.

   Additionally, by considering the effects of inverting the wind stress at the latitudes of the circumpolar connection, a clearly nonlinear dependence of the channel transport on the applied wind stress is revealed, while experiments with rather minor changes to the wind stress (e.g., McDermott 1996; Gnanadesikan and Hallberg 2000) suggest a nearly linear behavior.

Outside of frictional and inertial boundary layers, the transport across geostrophic contours is in an approximate balance with the JEBAR term. If, in addition, the shear transport is mostly zonal, the deep transport across geostrophic contours must be much smaller than the total transport across geostrophic contours. For blocked geostrophic contours, this implies that the total transport can to leading order be attributed to the shear transport, which provides a first-order estimate of the reaction of the ACC to changes in Southern Ocean hydrography. Through the effect of Ekman pumping on the density stratification this extends to the estimation of the reaction to changes in the wind stress field over the Southern Ocean.

Acknowledgments. We greatly appreciate helpful discussions with Matthias Prange, Vladimir Ivchenko, and Eberhard Fahrbach. Special thanks are also due to two anonymous reviewers whose constructive criticism helped to improve the paper a lot. This work was analyzed using the FERRET data visualization program, created and freely distributed by Steve Hankin of TMAP (http://www.wrc.noaa.gov/Ferret).

REFERENCES

Bryan, K., 1984: Accelerating the convergence to equilibrium of ocean–climate models. *J. Phys. Oceanogr.,* **14,** 666–673.

——, and L. J. Lewis, 1979: A water mass model of the world ocean. *J. Geophys. Res.,* **84,** 2503–2517.

Cai, W., and P. G. Baines, 1996: Interactions between thermohaline- and wind-driven circulations and their relevance to the dynamics of the Antarctic Circumpolar Current, in a coarse-resolution global ocean general circulation model. *J. Geophys. Res.,* **101,** 14 073–14 093.

Danabasoglu, G., and J. C. McWilliams, 1995: Sensitivity of the Global Ocean circulation to parameterizations of mesoscale tracer transport. *J. Climate,* **8,** 2967–2987.

Döös, K., and D. J. Webb, 1994: The Deacon cell and the other meridional cells of the Southern Ocean. *J. Phys. Oceanogr.,* **24,** 429–442.

Gent, P. R., and J. C. McWillams, 1990: Isopycnal mixing in ocean circulation models. *J. Phys. Oceanogr.,* **20,** 150–155.

——, J. Willebrand, T. J. McDougall, and J. C. McWillams, 1995: Parameterizing eddy-induced tracer transports in ocean circulation models. *J. Phys. Oceanogr.,* **25,** 463–474.

——, W. G. Large, and F. O. Bryan, 2001: What sets the mean transport through Drake Passage? *J. Geophys. Res.,* **106** (C2), 2693–2712.

Gerdes, R., C. Köberle, and J. Willebrand, 1991: The influence of numerical advection schemes on the results of ocean general circulation models. *Climate Dyn.,* **5,** 211–226.

Gill, A. E., and K. Bryan, 1971: Effects of geometry on the circulation of a three-dimensional southern hemisphere ocean model. *Deep-Sea Res.,* **18,** 685–721.

Gille, S. T., 1997: The Southern Ocean momentum balance: Evidence for topographic effects from numerical model output and altimeter data. *J. Phys. Oceanogr.,* **27,** 2219–2232.

Gnanadesikan, A., 1999: A simple predictive model for the structure of the oceanic pycnocline. *Science,* **283,** 2077–2079.

——, and R. W. Hallberg, 2000: On the relationship of the circum-

polar current to Southern Hemisphere winds in coarse-resolution ocean models. *J. Phys. Oceanogr.,* **30,** 2013–2034.
Goodman, P. J., 1998: The role of North Atlantic Deep Water formation in an OGCM's ventilation and thermohaline circulation. *J. Phys. Oceanogr.,* **28,** 1759–1785.
Hellerman, S., and M. Rosenstein, 1983: Normal monthly stress over the world ocean with error estimates. *J. Phys. Oceanogr.,* **13,** 1093–1104.
Hughes, C. W., and P. D. Killworth, 1995: Effects of bottom topography in the large-scale circulation of the Southern Ocean. *J. Phys. Oceanogr.,* **25,** 2485–2497.
Ivchenko, V. O., K. J. Richards, and D. P. Stevens, 1996: The dynamics of the Antarctic Circumpolar Current. *J. Phys. Oceanogr.,* **26,** 753–774.
——, A. E. Krupitsky, V. M. Kamenkovich, and N. C. Wells, 1999: Modeling the Antarctic Circumpolar Current: A comparison of FRAM and equivalent barotropic model results. *J. Mar. Res.,* **57,** 29–45.
Johnson, G. C., and H. L. Bryden, 1989: On the size of the Antarctic Circumpolar Current. *Deep-Sea Res.,* **36,** 39–53.
Krupitsky, A. E., and M. A. Cane, 1994: On topographic pressure drag in a zonal channel. *J. Mar. Res.,* **52,** 1–23.
——, V. M. Kamenkovich, N. Naik, and M. A. Cane, 1996: A Linear equivalent barotropic model of the Antarctic Circumpolar Current with realistic coastlines and bottom topography. *J. Phys. Oceanogr.,* **26,** 1803–1824.
Levitus, S., 1982: *Climatological Atlas of the World Ocean.* NOAA Prof. Paper 13, 173 pp. and 17 microfiche.
Losch, M., 2000: Analyse hydrographischer Schnitte mit Satellitenaltimetrie. Ph.D. ROM University of Bremen, Germany, 138 pp.
Macdonald, A. M., 1998: The global ocean circulation: A hydrographic estimate and regional analysis. *Progress in Oceanography,* Vol. 41, Pergamon, 281–382.
Maltrud, M. E., R. D. Smith, A. J. Semtner, and R. C. Malpme, 1998: Global eddy-resolving ocean simulations driven by 1985–1994 atmospheric winds. *J. Geophys. Res.,* **103,** 30 825–30 853.
Marshall, D., 1995: Topographic steering of the Antarctic Circumpolar Current. *J. Phys. Oceanogr.,* **25,** 1636–1650.
McDermott, D. A., 1996: The regulations of northern overturning by Southern Hemisphere winds. *J. Phys. Oceanogr.,* **26,** 1234–1255.
Mertz, G., and D. G. Wright, 1992: Interpretations of the JEBAR term. *J. Phys. Oceanogr.,* **22,** 301–305.
Munk, W. H., 1966: Abyssal recipes. *Deep-Sea Res.,* **13,** 707–730.
——, and E. Palmén, 1951: Note on the dynamics of the Antarctic Circumpolar Current. *Tellus,* **3,** 53–55.
Nowlin, W. D., Jr., and T. Whitworth III, 1977: Structure and transport of the Antarctic Circumpolar Current at Drake Passage from short-term measurements. *J. Phys. Oceanogr.,* **7,** 788–802.
——and J. M. Klinck, 1986: The physics of the Antarctic Circumpolar Current. *Rev. Geophys.,* **24** (3), 469–491.
Olbers, D. J., 1998: Comments on ''On the obscurantist physics of 'form drag' in theorizing about the Circumpolar Current.'' *J. Phys. Oceanogr.,* **28,** 1647–1654.
——, and C. Wübber, 1991: The role of wind an buoyancy forcing of the Antarctic Circumpolar Current. *Strategies for Future Climate Research,* M. Latif, Ed., Max-Planck-Institut für Meteorologie, 161–191.
——, and V. O. Ivchenko, 2001: On the meridional circulation and balance of momentum in the Southern Ocean of POP. *Ocean Dyn.,* **52,** 79–93.
Pacanowski, R. C., 1995: MOM 2 documentation user's guide and reference manual. GFDL Ocean Tech. Rep. 3, 232 pp.
Rahmstorf, S., and M. H. England, 1997: Influence of Southern Hemisphere winds on North Atlantic Deep Water Flow. *J. Phys. Oceanogr.,* **27,** 2040–2054.
Rattray, Jr., M., and J. G. Dworski, 1978: The effect of bathymetry on the steady baroclinic ocean circulation. *Dyn. Atmos.–Oceans,* **2,** 321–339.
Rintoul, S. R., and J. L. Bullister, 1999: A late winter hydrographic section from Tasmania to Antarctica. *Deep-Sea Res.,* **46,** 1417–1454.
——, and S. Sokolov, 2001: Baroclinic transport variability of the Antarctic Circumpolar Current south of Australia (WOCE repeat section SR3). *J. Geophys. Res.,* **106** (C2), 2815–2832.
——, C. Hughes, and D. Olbers, 2001: The Antarctic Circumpolar Current System. *Ocean Circulation and Climate,* G. Siedler et al., Eds., Academic Press, 271–302.
Samelson, R. M., 1999: Geostrophic circulation in a rectangular basin with a circumpolar connection. *J. Phys. Oceanogr.,* **29,** 3175–3184.
Smith, R. D., J. K. Dukowicz, and R. C. Malone, 1992: Parallel ocean general circulation modeling. *Physica D,* **60,** 38–61.
Stevens, D. P., and V. O. Ivchenko, 1997: The zonal momentum balance in an eddy-resolving general-circulation model of the Southern Ocean. *Quart. J. Roy. Meteor. Soc.,* **123,** 929–951.
Toggweiler, J. R., and B. Samuels, 1995: Effect of Drake Passage on the global thermohaline circulation. *Deep-Sea Res.,* **42,** 477–500.
——, and ——, 1998: On the oceans large-scale circulation near the limit of no vertical mixing. *J. Phys. Oceanogr.,* **28,** 1832–1852.
Treguier, A. M., and J. C. McWilliams, 1990: Topographic influences on wind-driven, stratified flow in a β-plane channel: An idealized model for the Antarctic Circumpolar Current. *J. Phys. Oceanogr.,* **20,** 321–343.
Vallis, G. K., 2000: Large-scale circulation and production of stratification: Effects of wind, geometry, and diffusion. *J. Phys. Oceanogr.,* **30,** 933–954.
Völker, C., 1999: Momentum balance in zonal flows and resonance of baroclinic Rossby waves. *J. Phys. Oceanogr.,* **29,** 1666–1681.
Wang, L., and R. X. Huang, 1995: A Linear homogeneous model of wind-driven circulation in a β-plane channel. *J. Phys. Oceanogr.,* **25,** 587–603.
Whitworth, T., III, 1983: Monitoring the transport of the Antarctic Circumpolar Current at Drake Passage. *J. Phys. Oceanogr.,* **13,** 2045–2057.
——, and R. G. Peterson, 1985: Volume transport of the Antarctic Circumpolar current from bottom pressure measurements. *J. Phys. Oceanogr.,* **15,** 810–816.
——, W. D. Nowlin Jr., and S. J. Worley, 1982: The net transport of the Antarctic Circumpolar Current through Drake Passage. *J. Phys. Oceanogr.,* **12,** 960–971.
Wolff, J.-O., E. Maier-Reimer, and D. J. Olbers, 1991: Wind-driven flow over topography in a zonal β-plane channel: A quasigeostrophic model of the Antarctic Circumpolar Current. *J. Phys. Oceanogr.,* **21,** 236–264.
Yaremchuk, M., N. L. Bindoff, J. Schröter, D. Nechaev, and S. R. Rintoul, 2001: On the zonal and meridional circulation and ocean transport between Tasmania and Antarctica. *J. Geophys. Res.,* **106** (C2), 2795–2814.